RSC Advances

PAPER



Cite this: *RSC Adv.*, 2026, **16**, 27634

# Stable dry reforming of methane over Ni–Pt bimetallic catalysts supported on KIT-5 in a continuous flow system

Mohammad Khalid,[ab] Ghadah Shukri Albakri,[c] S. Ganesan,[d] T. Vinod Kumar,[e] S. Padmanabhan,[f] Maha Awjan Alreshidi,[g] G. Sasikumar,[h] T. Anand,[i] Ahmed M. Fallatah,[j] Krishna Kumar Yadav, *[kl] Fehmi Boufahja,[m] Kamal Y. Thajudeen[n] and A. Subramani *[o]

Nanostructured bimetallic Ni–Pt catalysts supported on KIT-5 mesoporous silica were developed and assessed for their efficiency in the continuous dry reforming of methane (DRM) to generate synthesis gas. Both monometallic variants (Ni/KIT-5 and Pt/KIT-5) and a range of bimetallic Ni–Pt/KIT-5 catalysts were synthesized using co-impregnation and sequential impregnation methods. Comprehensive characterization of the catalysts was conducted through techniques such as high-resolution scanning electron microscopy (HR-SEM), X-ray diffraction (XRD), Brunauer–Emmett–Teller (BET) surface area analysis, thermogravimetric analysis (TGA), and Fourier-transform infrared spectroscopy (FT-IR). In the monometallic Ni-based catalysts, nickel primarily existed in the form of NiO. In contrast, the bimetallic catalysts exhibited surface species such as $Ni_2O_3$ and $NiPt_2O4$. In the bimetallic Ni–Pt catalysts, thermally stable $PtO_2$ and $NiPt_2O_4$ phases were identified. Reduction in hydrogen led to the development of Ni–Pt alloy phases on the surface, which enhanced the overall catalytic performance. The bimetallic Ni–Pt catalysts outperformed their monometallic counterparts in DRM activity. The nanofibrous structure of KIT-5, characterized by its interconnected pore network, provided improved accessibility to active sites and facilitated efficient diffusion of reactants and products. Among the catalysts evaluated, the 9.5%Ni–0.5%Pt/KIT-5 composition achieved the highest conversions of both methane and carbon dioxide, while maintaining a relatively low $H_2$/CO product ratio. Durability assessments at 700 °C over a period of six hours demonstrated high thermal stability and negligible deactivation due to carbon deposition. Post-reaction analyses of the spent catalysts using XRD and HR-SEM revealed minimal structural deterioration. TGA measurements indicated that carbon deposition resulted in approximately 10% weight loss, suggesting the presence of mainly amorphous carbon and confirming the catalyst's excellent resistance to coking. The fibrous architecture of KIT-5 effectively suppressed nickel particle sintering and carbon build-up. These findings underscore the potential of Ni–Pt/KIT-5 systems, particularly with optimized metal loadings, as robust and coke-resistant catalysts for syngas production *via* dry reforming of methane.

Received 5th April 2026
Accepted 10th May 2026

DOI: 10.1039/d6ra02861f

rsc.li/rsc-advances

[a]*Department of Pharmaceutics, College of Pharmacy, King Khalid University, Asir-Abha 61421, Saudi Arabia*

[b]*Department of Chemistry, Graphic Era (Deemed to be) University, Dehradun-248002, Uttarakhand, India*

[c]*Department of Teaching and Learning, College of Education and Human Development, Princess Nourah Bint Abdulrahman University, P.O. Box 84428, Riyadh, 11671, Saudi Arabia*

[d]*Department of Mechanical Engineering, Sathyabama Institute of Science and Technology, Chennai, India*

[e]*Vels Institute of Science, Technology and Advanced Studies (VISTAS), Chennai, India*

[f]*Department of Mechanical Engineering, Vel Tech Rangarajan Dr. Sagunthala R&D Institute of Science and Technology, Chennai, Tamil Nadu, India*

[g]*Department of Chemistry, College of Science, University of Ha'il, Ha'il 81451, Saudi Arabia*

[h]*Department of Chemistry, St. Joseph's College of Engineering, OMR, Chennai, 600119, India*

[i]*Department of Chemistry, Sathyabama Institute of Science and Technology, Chennai, India*

[j]*Department of Chemistry, College of Science, Taif University, P.O. Box 11099, 21944, Taif, Saudi Arabia*

[k]*Department of VLSI Microelectronics, Saveetha School of Engineering, Saveetha Institute of Medical and Technical Sciences (SIMATS), Saveetha University, Chennai 602105, Tamil Nadu, India*

[l]*Environmental and Atmospheric Sciences Research Group, Scientific Research Center, Al-Ayen University, Nasiriyah, Thi-Qar, Iraq*

[m]*Biology Department, College of Science, Imam Mohammad Ibn Saud Islamic University (IMSIU), Riyadh, 11623, Saudi Arabia*

[n]*Department of Pharmacognosy, College of Pharmacy, King Khalid University, Abha, 62529 Saudi Arabia*

[o]*Department of Chemistry, Dwaraka Doss Goverdhan Doss Vaishnav College (Autonomous) (Affiliated to the University of Madras, Chennai), 833, Gokul Bagh, E.V.R. Periyar Road, Arumbakkam, Chennai 600 106, Tamil Nadu, India. E-mail: subuchem71@gmail.com*

# 1. Introduction

Global energy demand continues to rise, intensifying concerns over climate change due to greenhouse gas emissions from fossil fuels.[1] Meanwhile, crude oil reserves the dominant energy source are depleting rapidly, prompting increased interest in hydrogen as a cleaner alternative.[2] Tackling emissions while utilizing their energy potential offers a promising path to address both environmental and energy challenges.[3] Carbon dioxide removal from major emission sources and the atmosphere could be crucial in limiting future global warming. While no single solution exists, a combination of chemical, biological, and natural carbon sinks is essential.[4] Recycled or underground carbon may also serve as a substitute for fossil-based energy.[5]

A more sustainable method of using greenhouse gases is dry reformation of methane (DRM), thereby turns methane along with $CO_2$ directly into synthesized gas ($H_2$ and CO).[6] Unlike steam methane reforming (SMR), DRM is more suitable for water-scarce areas such as remote oil and gas fields. It also produces a lower $H_2$/CO ratio, ideal for Fischer–Tropsch applications like oxo-alcohol, acetic acid, and dimethyl ether production.[7,8] As climate concerns grow, research has shifted toward $CO_2$-based reforming, focusing on catalyst development and reaction mechanisms.[9] Though still early in commercialization, processes like CALCOR and SPARG show potential. Recently, BASF and Linde advanced the field with SYNSPIRE™ G1e110 and the DRYREF™ process, combining DRM with SMR for efficient syngas production.[10] Dry catalytic reforming of methane commonly employs supported noble metals or transition metals like nickel and cobalt as catalysts. Due to their high cost, noble metals are less practical for industrial use, while Ni and Co offer a cost-effective and efficient alternative for syngas production. Supported Ni- and Co-based catalysts show strong potential for large-scale hydrogen generation.[11–13] In addition to the primary $CH_4$–$CO_2$ process, the composition of syngas is further influenced by secondary reactions like CO disproportionation, steam reforming, reverse water-gas shift, and methane breakdown.[14]

The dry catalytic reforming of methane (DRM) is an energetically demanding reaction, with an enthalpy change of approximately 247.3 kJ $mol^{-1}$.[15] This high energy requirement stems from the inherent stability of methane and carbon dioxide molecules, making elevated temperatures typically around 1273 K essential for achieving efficient conversion, particularly under equimolar $CH_4$/$CO_2$ conditions.[16] The reaction environment is further complicated by various side reactions, including the Boudouard reaction, methane decomposition, reverse carbon oxidation, as well as the water-gas shift reaction reversed.[17] One of the most significant challenges is turning on $CO_2$, which tends to be less reactive and preferentially binds to basic sites on the catalyst.[18] Mechanistic pathways proposed for DRM generally adhere to models such as Langmuir–Hinshelwood–Hougen–Watson or Eley–Rideal, where the initial step involves adsorption of the reactants onto the catalyst surface.[19] Methane typically undergoes a stepwise dehydrogenation process, generating surface-bound intermediates such as $CH_3$*, $CH_2$*, CH*, and eventually carbon species (C*), which often dictate the reaction rate.[20] Simultaneously, $CO_2$ is activated through dissociative adsorption, producing surface-bound CO and oxygen species that help remove deposited carbon. Additional reactive intermediates like OH*, COOH*, and HCOO* contribute to oxidation steps on the catalyst surface.[21] The overall performance of the DRM process is closely tied to the properties of the catalyst support, particularly the presence of basic sites that enhance $CO_2$ activation and maintain catalyst stability.[22]

Carbon accumulation remains a significant challenge in reforming reactions, particularly with nickel-supported catalysts, as it leads to deactivation by blocking active sites and impeding reactor flow. Major contributors to carbon deposition include methane cracking and the Boudouard reaction.[23] To mitigate this, strategies such as methanation, gasification, and promotion of the reverse Boudouard reaction have been employed.[24] Cobalt aluminate ($CoAl_2O_4$)-based catalysts have shown promise in facilitating this reverse reaction *via* synergistic Langmuir–Hinshelwood and Mars–van Krevelen mechanisms.[25] Carbon forms through both gas-phase pyrolysis and surface-mediated reactions. At lower temperatures, the Boudouard reaction dominates, while methane decomposition is more prominent at higher temperatures.[26] Among carbon types, graphitic carbon is the most stable, though filamentous carbon species such as multi-walled carbon nanotubes (MWCNTs) can form on nickel surfaces during methane decomposition. The formation of such carbon structures is a well-known deactivation pathway in dry reforming of methane, as they can disrupt metal–support interactions and lead to catalyst instability. Therefore, suppressing the formation of these carbon species is critical, and the present study focuses on improving coke resistance through Ni–Pt bimetallic catalysts supported on KIT-5.[27] Enhancing these interactions and incorporating secondary metals like cobalt can significantly improve catalyst stability and suppress coke formation.[28]

Among the various strategies to improve the resistance of nickel-based catalysts to carbon deposition, the choice of support material is particularly important.[29] An effective support not only facilitates uniform dispersion of nickel species but also contributes to catalyst longevity through strong interactions with the metal phase.[30] Nickel has been supported on a range of metal oxides, including MgO,[31] $Al_2O_3$,[32] $SiO_2$,[33] $TiO_2$,[34] $La_2O_3$,[35] $CeO_2$,[36] and $ZrO_2$,[37] to enhance performance in the dry reforming of methane (DRM). Nanoporous materials have garnered interest as supports in recent advancements because of their capacity to inhibit coke production and stop nickel particle agglomeration.[38] The high surface areas and adjustable pore designs of supports such as MCM-41, mesoporous silica, dendritic fibrous nanosilica, SBA-15, SBA-16, mesostructured alumina and wide-pore zeolites, have attracted attention in addition to typical oxides.[39–41] A noteworthy material in this category is KCC-1 (KAUST Catalysis Center-1), a fibrous silica introduced in 2011. KIT-5, another fibrous silica with a distinctive spherical morphology, features radially oriented fibers and a highly open porous structure. It has a large pore capacity

($\sim$2.18 $cm^3\ g^{-1}$) and an extensive surface area ($\sim$1244 $m^2\ g^{-1}$).[42] The architecture, made up of concentric silica fibers with dimensions ranging from 1–250 nm in length and 1–10 nm in diameter, promotes rapid molecular diffusion and minimizes internal mass transfer limitations common in traditional supports.[43,44]

Although KIT-5 has primarily been studied in areas such as drug delivery, gas adsorption, and heterogeneous catalysis, its potential in DRM remains underexplored. Due to its dendritic morphology, thermal robustness, low acidity, and resistance to sintering, KIT-5 presents a promising option for reforming reactions.[45,46] These characteristics enhance metal dispersion and $CO_2$ adsorption both of which are vital for achieving high catalytic activity and selectivity in DRM. While research on KIT-5-based systems in this reaction is still in its early stages, some findings have been encouraging.[47] For instance, Ni–La/KIT-5 has shown decreased carbon accumulation, and Ni/KIT-5 has demonstrated potential in methane partial oxidation, suggesting broader applicability of this support in reforming technologies.[48]

Since the two metals interact favourably, bimetallic catalysts frequently perform better than their monometallic counterparts, particularly at temperatures between 500 and 800 °C. These enhancements stem from improved dispersion of active sites, the formation of stable alloys, and reinforced interactions with the support material.[49] Adding a secondary transition metal to nickel-based catalysts has shown significant potential in reducing carbon build-up. While noble metals such as Rh, Pt, Pd, and Ru deliver excellent catalytic results, their expense limits widespread application.[50–53] Consequently, attention has turned to more economical options, with cobalt gaining recognition as an effective and budget-friendly co-catalyst. For instance, in contrasted with single-metal systems, Zhang *et al.* found that Ni–Pt catalysts exhibited better activity and endurance over the production of coke and structural breakdown.[51,54]

This work explores the application of KIT-5 provides an anchor for bimetallic Ni–Pt catalysts in DRM with the goal of creating a high conversion, selectivity, as well as coke-resistant catalyst which is thermally stable. Ni–Pt/KIT-5 catalysts were prepared by co-impregnation and characterized to understand their physicochemical properties. Their performance was evaluated under DRM conditions to assess activity, stability, and syngas yield. While Ni–Pt catalysts on various supports have been widely studied, their application on KIT-5 remains unexplored.[55,56] The study also examines the impact of KIT-5 and Ni–Pt interactions on catalyst durability, with post-reaction analysis used to evaluate carbon deposition.

## 2. Catalytic activity

A stainless-steel fixed-bed flow reactor was used to evaluate catalytic performance was manufactured by High-Tech Industries, Mumbai, India, the catalytic efficiency of the synthesized materials for dry reforming of methane (DRM) was assessed. The reactions were conducted between 300 and 800 °C at atmospheric pressure. In order to establish a steady bed, about 200 mg of catalysts was placed within the reactor and stabilized at both ends by quartz wool. A K-type thermocouple was positioned near the catalyst to accurately measure the reaction temperature. The catalyst was reduced in a hydrogen environment (20 mL $min^{-1}$) at 700 °C for two hours to activate it before starting the reforming operation. After reduction, the reactant vapor was added after the reactor had cooled to 300 °C. The feed was made up of a 1 : 1 molar ratio of carbon dioxide and methane, diluted with nitrogen, and fed at a total flow rate of 50 mL $min^{-1}$, which corresponds to a gaseous hourly space velocity (GHSV) about 36 000 mL $g^{-1}\ h^{-1}$. Under the experimental conditions, control tests verified that none of the reactor's constituents, including quartz wool, contributed to any catalytic activity. The composition of the product gas was periodically checked *via* a SHIMADZU GC-2014 gas chromatograph fitted with a 2 m SHINCARBON ST column and a thermal conductivity detector (TCD). A six-port VICI Valco nozzle equipped with a 1 mL sampling loop was used to inject gas samples.

The following computations were used to calculate the breakdown frequency of methane (TOF($CH_4$)), the resulting conversions of $CH_4$ and $CO_2$, and the $H_2$/CO product ratio.

$$\%\ CH_4\ \text{conversion} = \frac{\text{moles of } CH_4\ (\text{in}) - \text{moles of } CH_4\ (\text{out})}{\text{moles of } CH_4\ (\text{in})} \times 100 \quad (1)$$

$$\%\ CO_2\ \text{conversion} = \frac{\text{moles of } CO_2\ (\text{in}) - \text{moles of } CO_2\ (\text{out})}{\text{moles of } CO_2\ (\text{in})} \times 100 \quad (2)$$

$$\frac{H_2}{CO} = \frac{\text{moles of } H_2 \text{ produced}}{\text{moles of CO produced}} \quad (3)$$

$$TOF_{CH_4} = \frac{\text{moles of } CH_4\ (\text{in})}{60 \times 60 \times m_{Ni}} \quad (4)$$

The molar quantities of methane and carbon dioxide at the reactor inlet are denoted as $CH_4$ in and $CO_2$ in, respectively, while $n$$CH_4$ out and $n$$CO_2$ out represent their corresponding molar amounts at the reactor outlet. The term $m_{Ni}$ refers to the number of moles of surface-exposed nickel atoms.

### 2.1. Synthesis of KIT-5

KIT-5 mesoporous silica was synthesized following a refined method adapted from established literature.[57] Initially, a combination consisting of 9.7 g of 36% hydrochloric acid along with 198 g of deionized water was used to dissolve 21.5 g of the non-ionic components' triblock copolymer Pluronic F127. To achieve total homogeneity, the resultant solution was continuously agitated for five hours at 45 °C. After this, 21.5 g of tetraethyl orthosilicate (TEOS) was introduced as the silica precursor, and the reaction mixture was stirred under identical conditions overnight to promote condensation and self-assembly. After that, the synthesis gel underwent a 24 hour

hydrothermal aging procedure at 100 °C. Once the product had cooled, it was filtered to recover the solid, properly cleaned with distilled water in order to get rid of any remaining acidic substances along with surfactant, and then allowed to dry naturally. Finally, to produce the mesoporous structure and remove the organic template, the material was calcined with air at 550 °C for five hours at a ramp rate of 2 °C per minute.

### 2.2. Impregnation of nickel and platinum metal on KIT-5

Ni (9 wt%) and Pt (1 wt%) bimetallic catalysts supported on KIT-5 were synthesized *via* a co-impregnation method. In this procedure, predetermined amounts of nickel nitrate and hexachloroplatinic acid were dissolved in deionized water to prepare the metal precursor solution. This solution was then impregnated onto the pre-synthesized KIT-5 support and stirred continuously for 5 hours. The mixture was subsequently dried at 120 °C, followed by calcination at 550 °C for 5 hours. The obtained catalyst was ground and sieved to a particle size of 20–40 mesh. Prior to catalytic testing, the packed catalyst bed was subjected to an *in situ* reduction treatment under a hydrogen stream (20 mL $min^{-1}$) at 600 °C for 2 hours. Fig. 1 illustrates the preparation process of Ni–Pt bimetallic catalysts supported on KIT-5, highlighting each step involved in their synthesis and structural integration.

### 2.3. Catalyst characterization techniques used

The structural features of the synthesized materials were analyzed using various advanced characterization techniques. A Rigaku D/Max-2500/PC diffractometer using Cu-Kα radiation was used to perform powder X-ray diffraction (XRD) at 40 kV and 250 mA. The low-angle patterns in XRD were obtained in the 2$\theta$ range of 0.5° to 4° in order to evaluate mesostructural ordering. Textural properties were assessed by employing the Micromeritics ASAP 2020 analyzer in nitrogen adsorption–desorption studies at −196 °C. To remove surface-bound pollutants, samples were vacuum degassed for five hours at 200 °C before to testing. Specific surface area was estimated using the Brunauer–Emmett–Teller (BET) technique, and the adsorption isotherm data was utilized to calculate the total pore volume. Pore size distributions were determined as part of the desorption branch using the Barrett–Joyner–Halenda (BJH) method. Fourier-transform infrared (FT-IR) spectroscopy with an AVATAR-360 device was used to investigate surface functional groups. $NH_3$-TPD setup with a thermal conductivity detector (TCD) was used to investigate the acidic nature of the

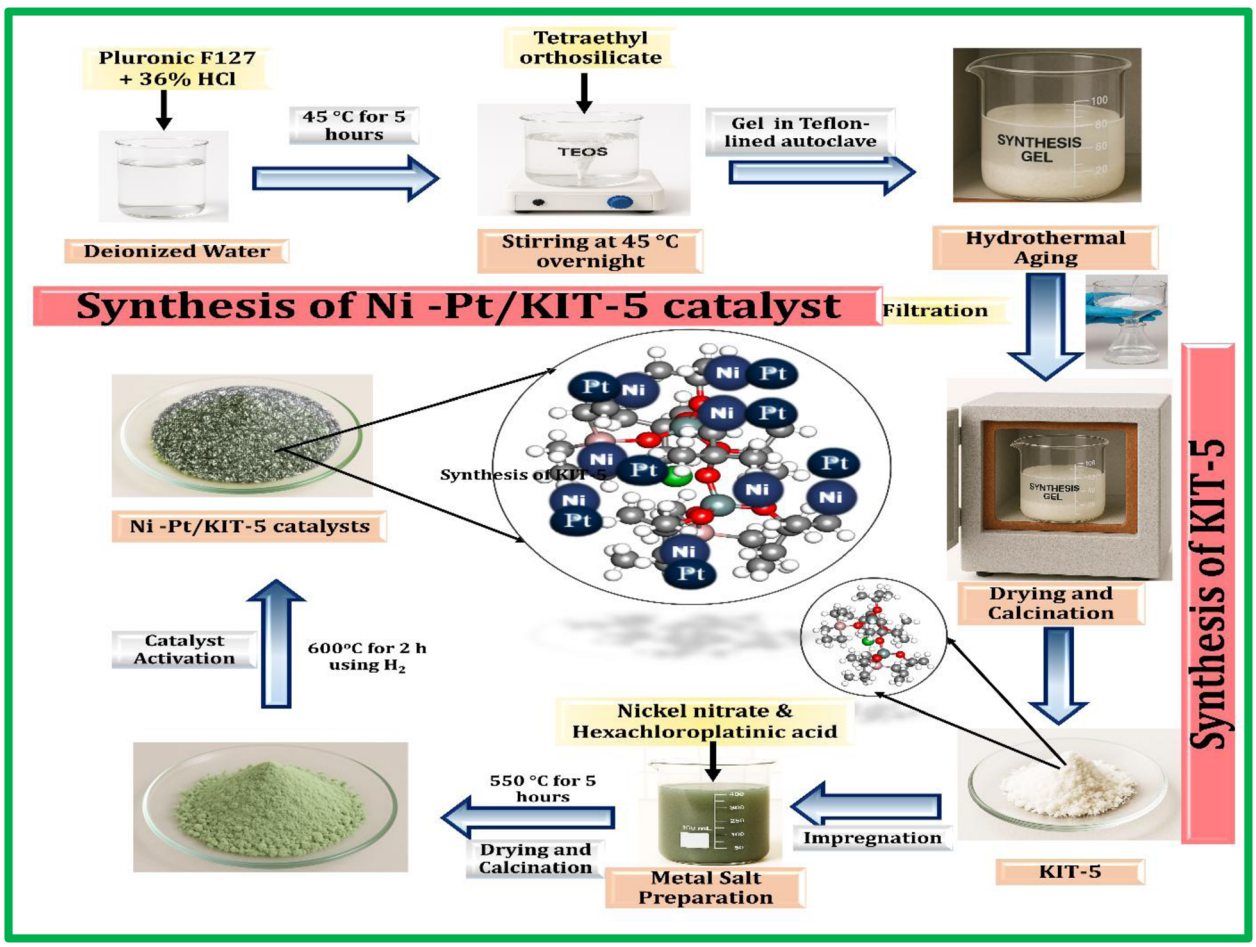


Fig. 1 Shows the synthesis of Ni–Pt bimetallic catalysts supported on KIT-5.

catalysts. The samples were heated under helium from 100 °C to 550 °C at a rate of 10 °C per minute in order to eliminate weakly bound species before $NH_3$ adsorption. Ammonia was then introduced at 100 °C for 30 minutes, followed by temperature ramping to 700 °C at the same rate to monitor desorption behavior. These analyses followed modified versions of well-documented procedures in the literature.

# 3. Catalyst characterization

## 3.1. Low angle XRD

The low-angle patterns in XRD of the Ni–Pt/KIT-5 catalysts (Fig. 2A) display a prominent diffraction peak at approximately 0.7°, corresponding to the (111) plane, along with two weaker reflections around 0.8° and 1.2°, which can be attributed to the (200) and (220) planes, respectively. The weak reflections between 1.5–2.5° correspond to higher-order diffraction peaks of the KIT-5 cubic Ia 3d mesostructure and do not indicate a separate crystalline phase. These reflections are characteristic of materials possessing a face-centered cubic (FCC) structure, typically associated with the *Fm3m* space group. A gradual increase in Pt content leads to peak broadening and reduced intensity, indicating a decline in the structural order of the mesoporous framework. Among the synthesized catalysts, the 9.5%Ni–0.5%Pt/KIT-5 and 9%Ni–1%Pt/KIT-5 compositions exhibited stronger diffraction peaks, suggesting more efficient Pt incorporation and better retention of the ordered mesostructure. In contrast, catalysts with higher Ni loading demonstrated a sharp decrease in the unit cell parameter ($a_0$), as shown in Table 1. This contraction may point to the formation of copper-like species or distortions within the structure. Notably, the initial expansion of the unit cell upon Ni addition could be linked to the substitution or interaction of Ni and Pt atoms within the silica framework, likely influenced by their differing atomic radii compared to $Si^{4+}$.[57]

## 3.2. High angle XRD

Fig. 2B shows the wide-angle XRD patterns of the synthesized catalysts. All samples exhibit a broad diffraction band centered at $2\theta \approx 22$–$23°$, which is characteristic of the amorphous silica framework of the KIT-5 support, indicating that the structural integrity of the support is preserved after metal incorporation. As observed in Fig. 2B, no well-defined diffraction peaks corresponding to crystalline NiO or Pt phases are distinctly visible. This suggests that the metal species are highly dispersed within the mesoporous framework and/or present as very small crystallites below the detection limit of XRD. The presence of weak and broadened features further supports the formation of poorly crystalline or nanosized metal species. With increasing metal loading, slight variations in the background profile and overall intensity can be observed in Fig. 2B, indicating subtle structural modifications and possible metal–support interactions. In the bimetallic samples, these changes may be associated with enhanced interaction between Ni, Pt, and the KIT-5 framework. The absence of distinct Pt-related reflections in Fig. 2B further confirms that Pt is finely dispersed, likely existing as nanosized clusters. Overall, the XRD results demonstrate that both Ni and Pt are well distributed within the KIT-5 support with high dispersion, which is advantageous for catalytic applications.

This interpretation is supported by complementary characterization results. The $H_2$-TPR profiles show a shift of Ni reduction peaks toward higher temperatures, indicating stronger interaction between Ni species and the support. Additionally, BET analysis reveals a decrease in surface area and pore volume upon metal loading, consistent with partial pore blocking or structural contraction. HR-TEM images further confirm that while the mesostructure is retained, metal nanoparticles are well dispersed within the framework, suggesting intimate contact between metal and support. In parallel, the

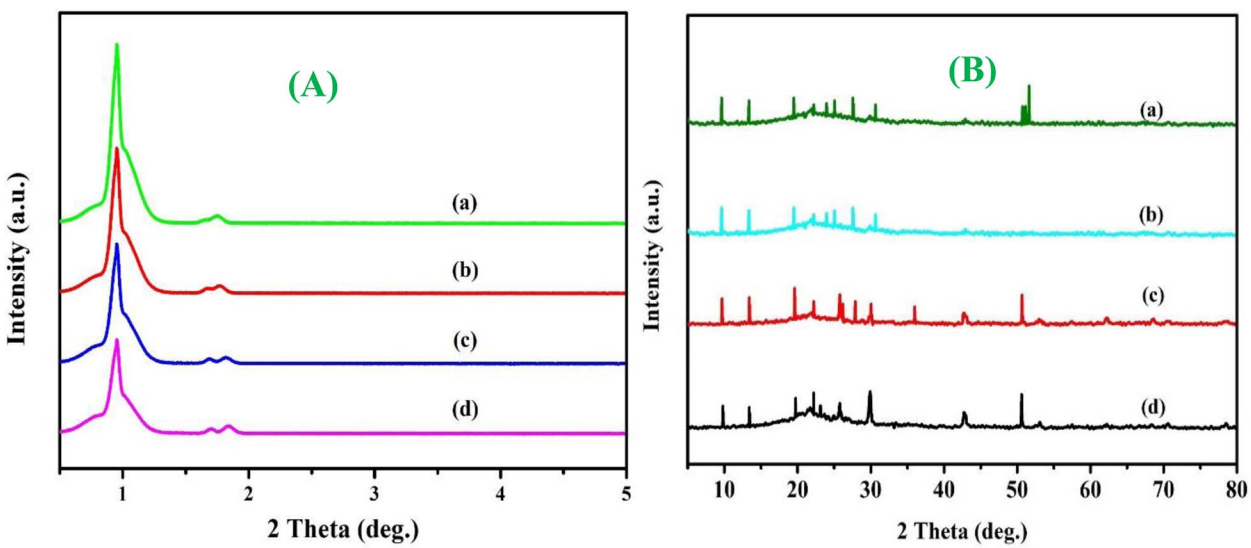


Fig. 2 (A) Low angle XRD patterns and (B) high angle XRD patterns of (a) Ni(10%)-KIT-5, (b) Pt(1%)-KIT-5, (c) Pt(0.5%)/Ni(9.5%)-KIT-5, and (d) Pt(1%)/Ni(9%)-KIT-5.

Table 1 Physiochemical properties and acidity of the catalysts Pt/Ni-KIT-5-catalyst

| Catalyst name | Surface area ($m^2\ g^{-1}$)[a] | $S_{micro}$ ($m^2\ g^{-1}$)[a] | $S_{ext}$ ($m^2\ g^{-1}$)[a] | $V_{total}$ ($cm^3\ g^{-1}$)[b] | $V_{micro}$ ($cm^3\ g^{-1}$)[b] | $V_{meso}$ ($cm^3\ g^{-1}$)[b] | Actual loading (wt%)[c] (Ni) | Actual loading (wt%)[c] (Pt) | dBJH (nm)[d] | Crystallite size (nm)[e] |
|---|---|---|---|---|---|---|---|---|---|---|
| Ni(10%)-KIT-5 | 802.11 | 423.12 | 378.99 | 0.812 | 0.590 | 0.222 | 9.8 | — | 8.6 | 12.7 |
| Pt(1%)-KIT-5 | 822.02 | 432.99 | 389.03 | 0.818 | 0.592 | 0.226 | — | 0.9 | 8.5 | 12.2 |
| Pt(0.5%)/Ni(9.5%)-KIT-5 | 685.66 | 366.77 | 318.89 | 0.549 | 0.324 | 0.225 | — | 0.51 | 7.6 | 9.45 |
| Pt(1%)/Ni(9%)-KIT-5 | 678.66 | 358.66 | 320 | 0.540 | 0.310 | 0.23 | 8.8 | — | 7.5 | 9.40 |

[a] Surface area obtained from BET isotherrm. [b] Pore volume obtained from BET isotherrm. [c] Theoretical Pt–Ni molar ratio, molar ratios. [d] Pore diameter (Dp) (desorption branch by BJH method) obtained from BET isotherrm. Determined by ICP-OES molar ratios values. [e] Average metal oxide crystal size was calculated by Scherrer equation.

stronger metal–support interaction promoted by Ni (and Ni–Pt) can generate interfacial Ni–O–Si linkages (nickel–silicate-like domains) that are typically poorly crystalline and present as broad/low-intensity XRD features. The combined effects are consistent with (i) the observed TPR shifts, indicating harder-to-reduce Ni species, and (ii) the textural changes reported below (BET/SEM). While the limited intensity precludes an unambiguous phase assignment by XRD alone, these data support the formation of crystalline $SiO_2$ domains and/or silicate-like interfacial species in the bimetallic samples. At higher nickel loadings (*e.g.*, 9.5 wt%), reflections attributed to monoclinic Pt (JCPDS 01-087-0640) emerge at $2\theta = 35°$, 38.7°, and 49.1°, suggesting the presence of platinum in a monoclinic phase. The absence of distinct Pt diffraction peaks and the reduced intensity of NiO reflections in bimetallic samples indicate high metal dispersion and possible formation of finely dispersed Ni–Pt alloy species. This is further supported by TPR results, where the presence of Pt facilitates the reduction of Ni species, suggesting hydrogen spillover and strong metal–metal interaction.[58] The 9%Ni–1%Pt/KIT-5 catalyst shows well-defined diffraction features, indicating a favorable metal distribution at this composition. However, further increases in Pt loading lead to less distinct crystalline peaks, likely due to high dispersion and reduced particle size, making phase identification more challenging.

### 3.3. BET analysis

The synthesized materials were extensively characterized for their textural properties through nitrogen adsorption–desorption ($N_2$-sorption) isotherm analysis, with corresponding data presented in Fig. 3 and Table 1. The isotherms for all samples were classified as type IV, featuring a wide-ranging H2-type hysteresis loop a distinctive hallmark of mesoporous materials possessing uniform yet large cage-like pores. This behavior affirms the successful synthesis of mesostructured frameworks with well-defined porosity across the entire series. In the case of the unmodified KIT-5 support, the isotherm profile distinctly indicated a highly developed mesoporous network. The material exhibited a pore diameter of approximately 8.5 nm, accompanied by a high nitrogen uptake capacity ranging between 0.60 and 0.85 $cm^3\ g^{-1}$, signifying the presence of a vast accessible surface area and interconnected pore system. The

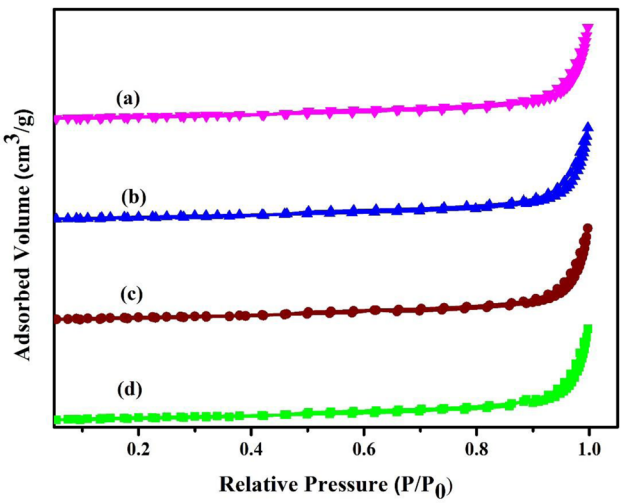


Fig. 3 $N_2$ adsorption–desorption isotherm (a) Ni(10%)-KIT-5, (b) Pt(1%)-KIT-5, (c) Pt(0.5%)/Ni(9.5%)-KIT-5, and (d) Pt(1%)/Ni(9%)-KIT-5.

BET surface area and total pore volume were notably high, measured at about 802.11 $m^2\ g^{-1}$ and 0.812 $cm^3\ g^{-1}$, respectively, confirming the exceptional porosity and structural integrity of the pristine KIT-5 framework. However, upon incorporation of nickel and platinum into the KIT-5 matrix, a pronounced alteration in the textural parameters was observed. Specifically, the BET surface area decreased to around 678.66 $m^2\ g^{-1}$, while the total pore volume reduced to approximately 0.540 $cm^3\ g^{-1}$. The main causes of this decrease in pore volume and surface area are possible structural distortion and partial pore blockage brought on by the addition of metal nanoparticles to the mesoporous channels. The decrease in BET surface area and BJH pore diameter observed after incorporation of Ni and Pt can be attributed to several factors. Firstly, metal nanoparticles are deposited within the mesoporous channels of KIT-5, leading to partial pore filling and blockage, which reduces accessible surface area. Secondly, strong metal–support interaction during calcination may induce slight framework contraction or pore wall thickening, resulting in reduced pore diameter. Additionally, the presence of Pt influences the dispersion of Ni species, leading to the formation of smaller metal particles that occupy internal pore space more

effectively. These combined effects contribute to the observed reduction in textural properties while still preserving the overall mesoporous structure. The emergence of the ~26–28° reflection in the Ni–Pt sample is attributed to partial occupation of mesopores by Ni and Pt nanoparticles along with structural contraction induced by strong metal–support interaction. This observation is consistent with XRD results, which indicate subtle structural modification upon metal incorporation. This provides a structural rationale for the larger decreases in SSA (specific surface area) and $V_{total}$ observed for Ni–Pt/KIT-5. The extent of this reduction showed a direct correlation with the metal loading higher concentrations of Ni and Pt led to more significant declines in porosity-related values. This trend suggests that as more metal was introduced, the internal mesoporous framework became increasingly filled or obstructed, possibly due to agglomeration or encapsulation of active metal species within the pores. ICP-OES was used to confirm the metal concentration. The exact metal loadings were found to be in close agreement with the nominal values, with actual loadings closely matching the nominal compositions (Ni ≈ 9–10 wt% and Pt ≈ 0.5–1 wt%). These findings indicate that the synthesis process was effective in achieving the targeted metal deposition, with negligible losses or leaching observed during preparation. The near-complete incorporation of metal precursors not only demonstrates the efficiency of the loading process but also reinforces the structural compatibility of the KIT-5 framework for hosting bimetallic species.[59] The reduction in crystallite size observed for bimetallic catalysts compared to monometallic Ni samples suggests improved dispersion of active metal species. This can be attributed to the presence of Pt, which inhibits Ni particle growth during calcination and promotes the formation of smaller, well-dispersed particles. The observed decrease in surface area and pore volume is consistent with increased metal loading and pore occupation, and does not indicate structural collapse, as confirmed by the preservation of mesoporous features in TEM and low-angle XRD results. The improved catalytic performance of Ni–Pt/KIT-5 catalysts can be directly correlated with their physicochemical properties. The reduced crystallite size and enhanced dispersion of metal particles, as observed from XRD and TEM analyses, provide a higher number of accessible active sites for methane activation. The shift in reduction temperature in TPR profiles indicates modified metal–support interaction, which facilitates the formation of active $Ni^0$ species at lower temperatures. Furthermore, the moderate decrease in surface area and pore volume reflects effective metal incorporation without significant loss of mesoporosity, ensuring efficient reactant diffusion. These combined effects contribute to enhanced catalytic activity and stability of the bimetallic catalysts. Despite the reduction in surface area and pore diameter, the preserved mesostructure and improved metal dispersion ensure sufficient accessibility of active sites, contributing to enhanced catalytic performance.[60,61]

### 3.4. TPR analysis

As illustrated in Fig. 4 the reduction properties of the synthesized catalysts were examined using Hydrogen-Temperature Programmed Reduction ($H_2$-TPR). The bimetallic 9%Ni–1%Pt/KIT-5 catalyst exhibits two main reduction peaks

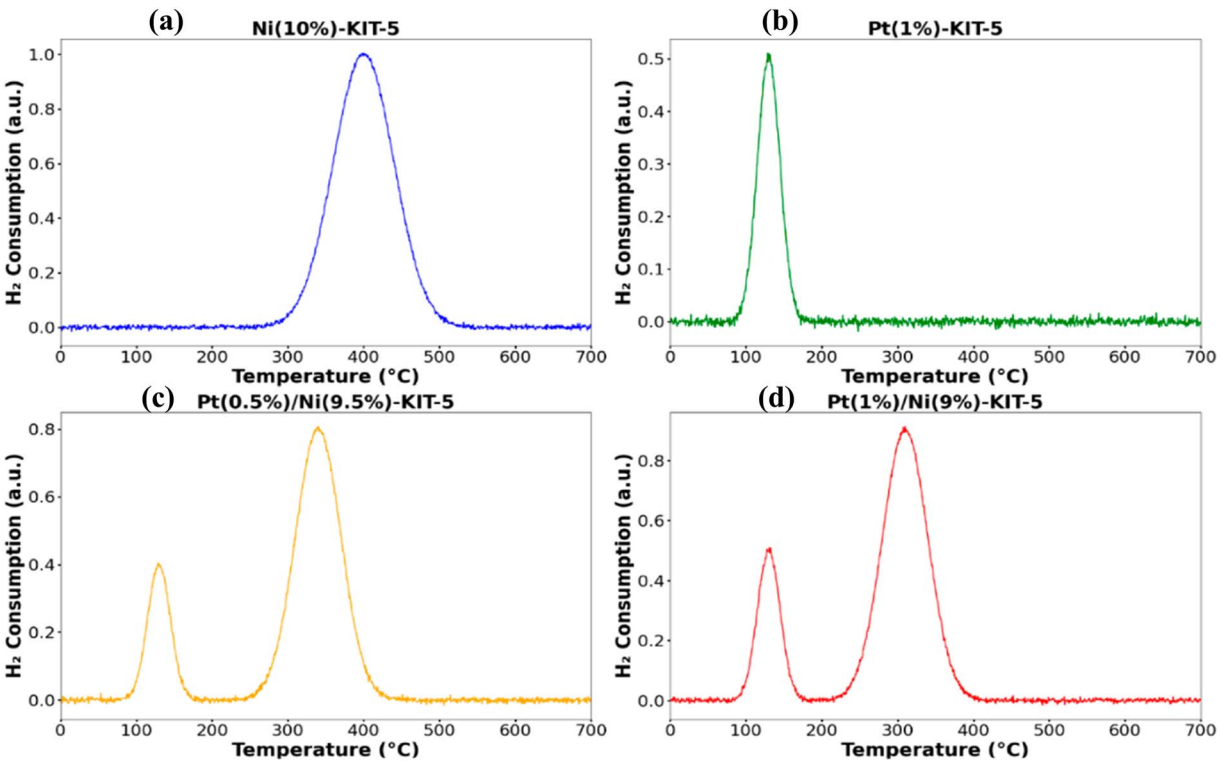


Fig. 4 TPR profile of (a) Ni(10%)-KIT-5, (b) Pt(1%)-KIT-5, (c) Pt(0.5%)/Ni(9.5%)-KIT-5, and (d) Pt(1%)/Ni(9%)-KIT-5.

corresponding to the reduction of Ni species. The low-temperature peak is associated with weakly interacting NiO species, while the high-temperature peak (around 500–600 °C) corresponds to strongly interacting Ni species reduced to metallic $Ni^0$. The exact peak positions have been verified from the TPR profiles and are consistent with literature reports for supported Ni catalysts. The broad nature of the reduction peaks and their partial overlap can reduce their visual prominence in the plotted profiles. This is particularly common for highly dispersed metal species, where reduction occurs over a wide temperature range rather than at sharp, well-defined peaks. This behavior implies good dispersion of nickel species on the KIT-5 support, facilitating a more efficient reduction. On the other hand, the monometallic Pt/KIT-5 sample displayed a reduction peak around 174 °C, associated with the conversion of $Pt^{2+}$ to $Pt^0$. When examining bimetallic catalysts with different Ni and Pt ratios, shifts in reduction temperatures and peak intensities were observed, suggesting changes in the redox properties due to interactions between the two metals. These observations indicate that the presence of Pt influences the reducibility of Ni species, as evidenced by the shift in reduction temperatures. This behavior is consistent with hydrogen spill-over and enhanced metal–metal interaction, which are commonly associated with improved catalytic performance. This effect became particularly noticeable when the Pt loading reached 1 wt%, where a consistent and stronger interaction was observed. However, increasing Pt content beyond 0.5 wt% altered the reduction pattern, resulting in the emergence of three separate reduction peaks likely due to Pt particle agglomeration and possible formation of bulk Pt phases. Among the tested formulations, the bimetallic Ni–Pt catalysts demonstrated the most favorable reduction characteristics, with hydrogen uptake occurring at comparatively lower temperatures, indicating improved reducibility. The hydrogen consumption data, summarized in Table 2 showed that monometallic Ni and Pt catalysts consumed 44 μmol $g^{-1}$ and 64 μmol $g^{-1}$ of hydrogen, respectively. For the bimetallic systems, hydrogen uptake increased with total metal content, ranging from 105 to 145 μmol $g^{-1}$. This trend confirms enhanced reducibility, likely driven by the cooperative effects between metal species and their interaction with the KIT-5 support. The observed reduction behavior is consistent with literature, where NiO supported on silica exhibits reduction peaks in the range of 300–700 °C depending on metal–support interaction strength.[62]

### 3.5. HR-TEM images

HR-Transmission Electron Microscopy (HR-TEM) provides critical insights into the atomic-scale structural characteristics of nanomaterials, making it an indispensable tool in characterizing mesoporous materials like KIT-5. In the HR-TEM images presented in Fig. 5(a) and 6(b), the unmodified KIT-5 support indicate the presence of a mesostructured framework characteristic of KIT-5. While long-range ordered pore channels are not distinctly resolved at lower magnifications, higher magnification images reveal regions consistent with mesoporosity. The overall morphology confirms that the mesoporous structure is largely retained after metal incorporation. This level of structural uniformity underscores the precise synthesis of KIT-5 and the robustness of its cubic symmetry. The consistently spaced mesoporous features inferred from contrast variations and supported by complementary low-angle XRD and BET analyses. The confirmation of mesoporosity is therefore based on a combination of characterization techniques, where low-angle XRD and $N_2$ sorption analysis provide stronger evidence for ordered mesostructure, while TEM supports the presence of dispersed metal particles within the framework. Following the incorporation of nickel and platinum nanoparticles, as shown in Fig. 5(c) and (d), the HR-TEM images reveal that the KIT-5 support largely retains its original mesoporous configuration. The framework remains well-defined and ordered, demonstrating that the metal loading process has minimal impact on the overall structural integrity of the support.[63] Within the mesoporous matrix, small, dark-contrast regions attributable to the Ni and Pt nanoparticles are uniformly dispersed, suggesting successful deposition without significant aggregation or pore blockage. The even distribution of metal particles across the support further highlights the compatibility of the impregnation method with the delicate mesostructure of KIT-5. The structural preservation after metal incorporation is corroborated by the continued presence of characteristic peaks in the low-angle XRD patterns and stable textural parameters in the $N_2$ sorption isotherms, collectively suggests that the mesostructural characteristics of KIT-5 are largely preserved, although some local structural modifications may occur upon metal loading throughout the synthesis and functionalization processes.[61,62] The uniform distribution of dark contrast nanoparticles within the KIT-5 framework provides direct evidence of improved metal dispersion in bimetallic catalysts compared to monometallic counterparts.

Table 2 Reduction nature, hydrogen consumption and quantity of acidity of (a) Ni(10%)-KIT-5 (b) Pt(1%)-KIT-5, (c) Pt(0.5%)/Ni(9.5%)-KIT-5 and (d) Pt(1%)/Ni(9%)-KIT-5.catalysts

| S. no. | Catalyst name | Reduction temperature (°C)[a] | Volume of $H_2$ consumption (μmol $g^{-1}$)[a] | Acidity (mmol $g^{-1}$) total[b] | *LT peak[b] | *HT Peak[b] |
|---|---|---|---|---|---|---|
| 1 | Ni(10%)-KIT-5 | 557 | 67 | 1.01 | 0.71 | 0.30 |
| 2 | Pt(1%)-KIT-5 | 150, 407 | 53 | 1.11 | 0.81 | 1.30 |
| 3 | Pt(0.5%)/Ni(9.5%)-KIT-5 | 319, 407 | 154 | 1.45 | 0.95 | 0.50 |
| 4 | Pt(1%)/Ni(9%)-KIT-5 | 274, 395 | 152 | 1.52 | 0.94 | 0.58 |

[a] Obtained and calculated from $H_2$-TPR profile. [b] Obtained from $NH_3$-TPD.

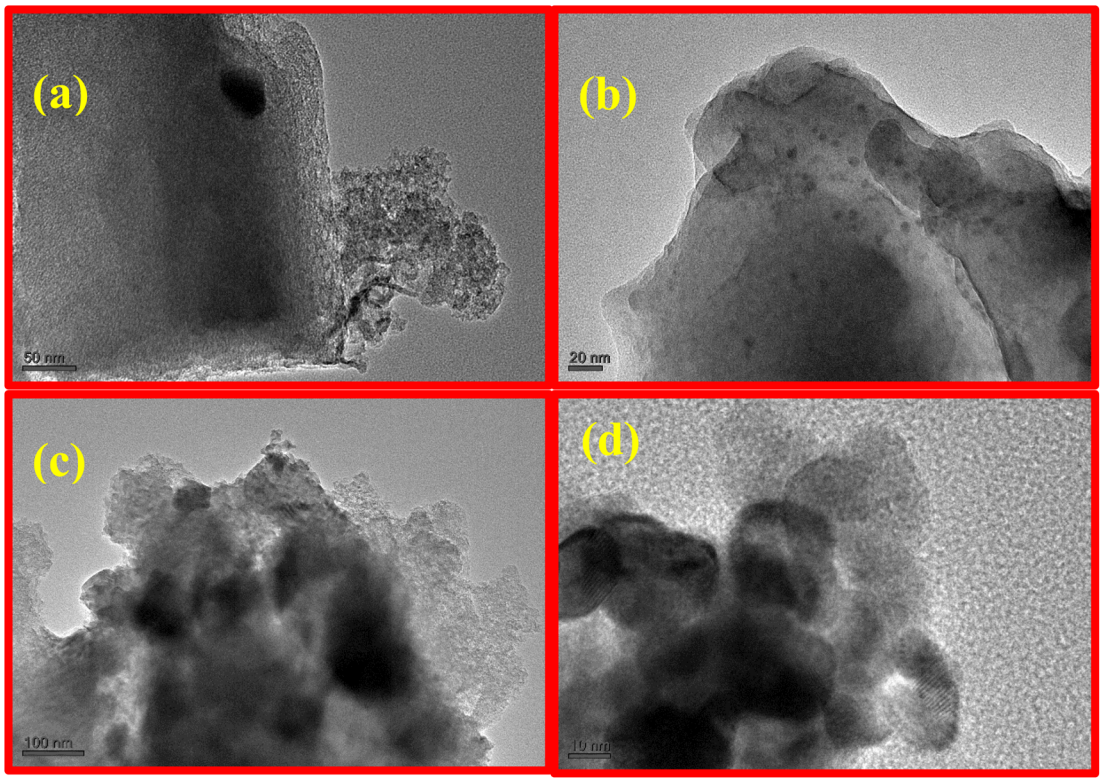


Fig. 5 HR-TEM images of (a) Ni(10%)-KIT-5, (b) Pt(1%)-KIT-5, (c) Pt(0.5%)/Ni(9.5%)-KIT-5, and (d) Pt(1%)/Ni(9%)-KIT-5.

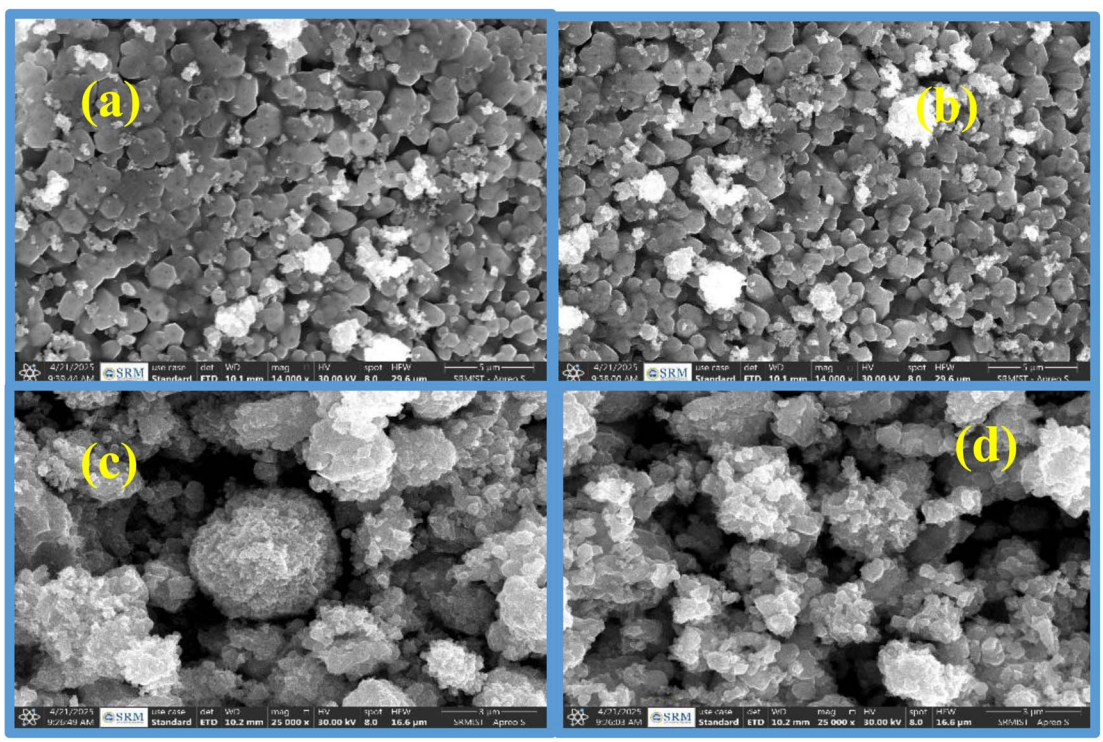


Fig. 6 HR-SEM images of (a) Ni(10%)-KIT-5, (b) Pt(1%)-KIT-5, (c) Pt(0.5%)/Ni(9.5%)-KIT-5, and (d) Pt(1%)/Ni(9%)-KIT-5.

### 3.6. HR-SEM images

Fig. 6(a–d) displays scanning electron microscopy (SEM) images that provide a comparative view of the surface morphology of the unmodified KIT-5 support and the KIT-5 catalyst after the incorporation of nickel and platinum. The pristine KIT-5, as shown in Fig. 6(a) and (b), exhibits a highly organized architecture, with distinct, cube-like slabs uniformly arranged in compact rectangular domains. These structures typically range in size from approximately 3.9 to 4.5 μm in length. Notably, the surface appears clean and well-defined, with no signs of particle agglomeration, indicating a stable mesoporous network with consistent textural features. In contrast, Fig. 6(c) and (d) illustrate the substantial morphological changes that occur following the deposition of Ni and Pt metals onto the KIT-5 framework. The once well-structured cubic morphology transforms into irregular, rounded, and partially spheroidal particles. Such Ni–Pt-induced silica ordering/silicate interfacial domains plausibly drive the transition toward rounded, denser particles seen by SEM, consistent with the textural losses measured by $N_2$ sorption. This change is accompanied by a notable reduction in particle dimensions, with the modified catalyst structures measuring between 1.4 and 2.5 μm. Despite this reduction in size, the particles remain dispersed, with no evidence of significant clustering or aggregation. The transition from a well-ordered cubic arrangement to a less uniform, rounded morphology upon metal loading signifies a clear structural impact induced by the incorporation of nickel and platinum. These modifications suggest that the metal impregnation disrupts the original mesostructure of KIT-5, potentially due to changes in surface energy, metal-support interactions, or partial pore collapse. Such morphological evolution plays a vital phase in influencing the catalytic behavior of the resulting material.[63]

### 3.7. $NH_3$-TPD analysis

The surface acidity properties of a range of bimetallic catalysts prepared with different ratios of nickel along with platinum anchored on KIT-5 mesoporous silica were methodically investigated using the ammonia-based temperature-programmed desorption ($NH_3$-TPD) methodology. Specifically, the study focused on catalysts with the nominal composition 9%Ni–1% Pt/KIT-5, with slight variations in metal loading to assess their impact on acid site distribution and strength. The resulting desorption patterns, as illustrated in Fig. 7 and summarized in Table 2, provided detailed insights into the concentration and nature of acid sites present on the catalyst surfaces. Since ammonia desorption from the catalyst surface takes place over a range of temperatures, acid sites can be divided into three groups: mild (between 100 and 250 °C), moderate (between 250 and 400 °C), and strong (beyond 400 °C). These acidic functionalities are typically associated with surface-bound species such as tetrahedrally coordinated silicon ($Si^{4+}$) and protonic hydrogen ($H^+$) embedded within the silica framework. The total acidity, as quantified from the area under the $NH_3$ desorption peaks, ranged from 1.50 to 1.80 mmol $NH_3$ per gram of catalyst across the different formulations. A key trend observed was the

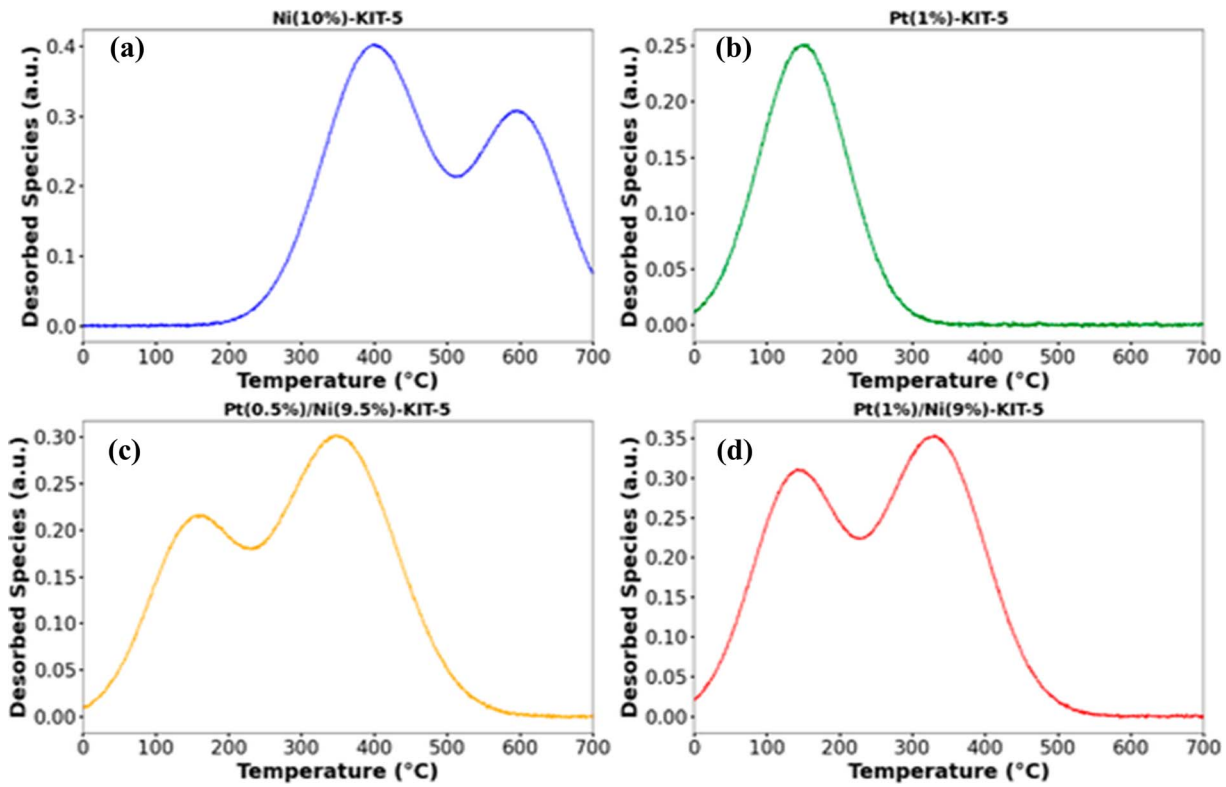


Fig. 7 TPD analysis of (a) Ni(10%)-KIT-5, (b) Pt(1%)-KIT-5, (c) Pt(0.5%)/Ni(9.5%)-KIT-5, and (d) Pt(1%)/Ni(9%)-KIT-5.

correlation between increasing platinum content and an enhancement in overall acidity. Similarly, a slight increase in nickel loading from 9 wt% to 9.5 wt% also resulted in greater acid site density. According to these findings, nickel and platinum both significantly influence the acidic conditions of the KIT-5 support, most likely by interacting *via* the silica framework and producing fresh acid sites. In certain formulations, the presence of no additional metal species other than Ni and Pt were present in the catalysts implicated in amplifying acidity, possibly by further modifying the surface electronic properties and introducing additional Lewis acid centers. Interestingly, while the 9.5%Ni–0.5%Pt/KIT-5 catalyst exhibited the highest measured total acidity, it did not correspond to the best catalytic performance. Instead, the 9%Ni–1%Pt/KIT-5 composition demonstrated superior activity in the target reaction, highlighting the complexity of the relationship between acidity and catalytic efficiency. This discrepancy underscores the importance of not only the quantity but also the quality and nature of acid sites. Parameters such as the Brønsted-to-Lewis acid site ratio, acid site strength, metal dispersion, and the structural integrity of the mesoporous framework are all integral to catalytic function. The enhanced performance of the 9%Ni–1%Pt/KIT-5 catalyst is likely due to a more optimal balance between metal content and acid site characteristics, facilitating better metal–support interaction, improved reactant activation, and resistance to deactivation mechanisms such as coke formation.[61] In contrast, the excessive acidity observed in the 9.5%Ni–0.5%Pt variant may promote undesirable side reactions or accelerate carbonaceous deposits, which are particularly detrimental in applications like biomass reforming or hydrodeoxygenation. The pronounced rounding and densification of the KIT-5 particles after Ni–Pt impregnation arises from metal-salt-induced silica condensation during calcination. The presence of $Ni^{2+}/Pt^{4+}$ species locally restructures the pore walls, resulting in partial collapse of the original fibrous morphology. This morphological transition decreases SSA and narrows pore mouths, which imposes diffusion limitations at high conversion. However, the same densification strengthens metal–support interaction and reduces Ni sintering, explaining why the bimetallic samples combine slightly weaker mass transport with superior long-term stability in DRM. Therefore, tuning metal ratios to achieve a Ni–Pt synergistic interaction, while maintaining a moderate and well-distributed acidic profile, appears critical for maximizing catalytic efficacy in such complex reactions. In DRM, moderate acid/amphoteric sites improve $CO_2$ activation and supply surface oxygen species that continually oxidise deposited carbon; thus the acidity trends observed for Ni–Pt catalysts correlate with both their superior reactivity and their reduced tendency for coke formation.

## 4. Catalytic activity of dry reforming

The Fig. 8A presents a detailed comparison of methane ($CH_4$) conversion efficiencies of various metal-supported KIT-5 catalysts namely Ni(10%)-KIT-5, Pt(1%)-KIT-5, and bimetallic Pt/Ni systems across a range of reaction temperatures. All of the

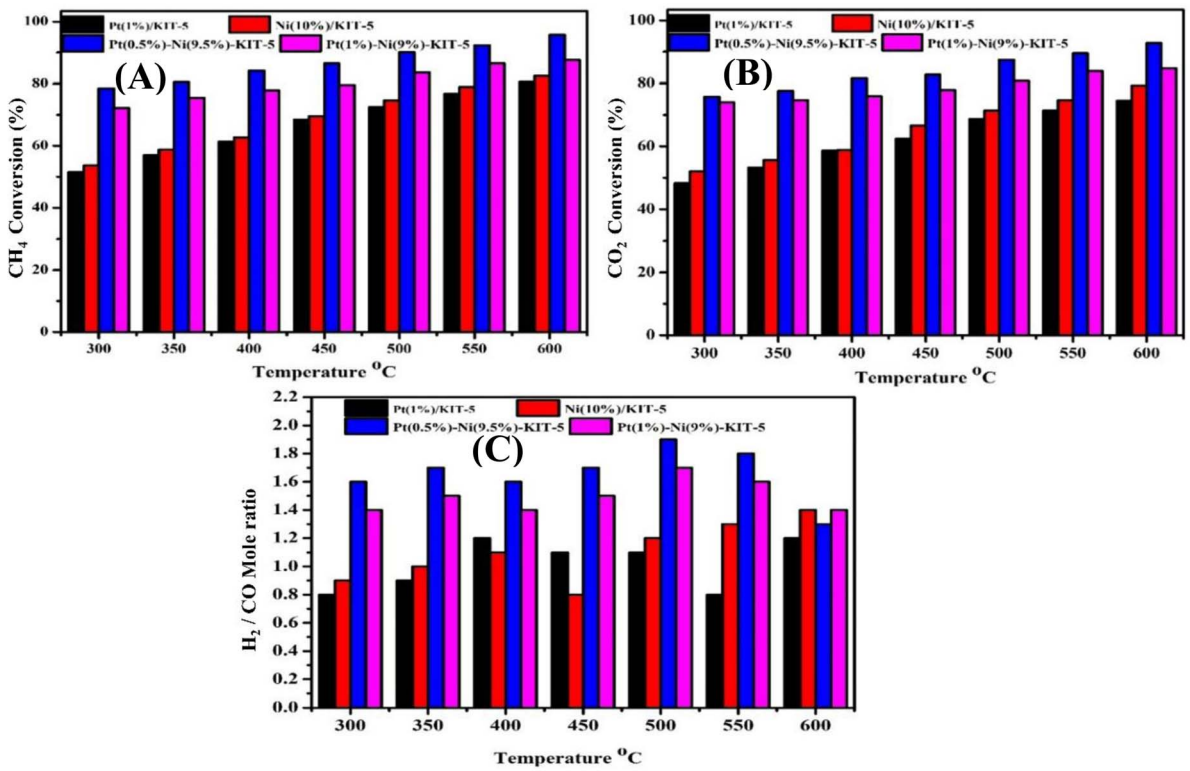


Fig. 8 (A) $CH_4$ conversion, (B) $CO_2$ conversion, and (C) $H_2$/CO ratio of Ni, Pt and Ni–Pt supported KIT-5 catalysts with reaction temperature. Reaction conditions: 3.2 g catalyst, GHSV 36,000 mL $g_{cat}^{-1}$ $h^{-1}$, and $CH_4/CO_2/N_2$ 1 : 1 : 3.

tests were conducted using 200 mg of catalyst, a feed gas composition of $CH_4/CO_2/N_2 = 1:1:3$, and a GHSV of 36 000 mL $g^{-1}$ $h^{-1}$. At the lowest tested temperature of 300 °C, the monometallic catalysts Pt(1%) and Ni(10%) showed $CH_4$ conversions of 51.5% and 53.6% respectively, indicating relatively low activity in the absence of significant thermal energy. However, the bimetallic catalysts, Pt(0.5%)/Ni(9.5%)-KIT-5 and Pt(1%)/Ni(9%)-KIT-5, significantly outperformed their monometallic counterparts at this temperature, achieving conversions of 78.5% and 72.2% respectively. This highlights the enhanced catalytic synergy when Pt and Ni are co-deposited on the KIT-5 support. This enhanced performance can be correlated with improved metal dispersion and modified reducibility observed in characterization studies, which facilitate more efficient methane activation and carbon removal. As the temperature increases, all catalysts exhibit a steady rise in $CH_4$ conversion. At 350 °C, Ni(10%) and Pt(1%) conversions increased to 58.7% and 56.9% respectively, while the bimetallic Pt(0.5%)/Ni(9.5%) and Pt(1%)/Ni(9%) systems already exhibit significantly higher conversions (80.5% and 75.5%) compared to monometallic catalysts, indicating enhanced low–temperature activity of the bimetallic systems. At 350 °C, the superior performance of bimetallic Ni–Pt catalysts can be attributed to improved reducibility and metal–metal interaction. The presence of Pt facilitates hydrogen spillover, promoting the reduction of NiO to active $Ni^0$ species at lower temperatures, as supported by TPR results. Additionally, Pt enhances $CO_2$ activation and oxygen mobility, which helps remove surface carbon species and maintain active sites. These combined effects enable the bimetallic catalysts to achieve higher conversions even at relatively low temperatures compared to monometallic systems. The improved low-temperature activity observed in catalytic tests (*e.g.*, at 350 °C) is consistent with the enhanced reducibility of bimetallic catalysts observed in TPR profiles. This performance gap widens further with temperature. At 400 °C, Ni(10%) reaches 62.7% and Pt(1%) 61.4%, whereas the bimetallic catalysts improve to 84.2% for Pt(0.5%)/Ni(9.5%) and 77.8% for Pt(1%)/Ni(9%). At 450 °C, the monometallic Ni and Pt catalysts deliver 69.6% and 68.5% conversions respectively, whereas the Pt/Ni systems further rise to 86.5% and 79.6%. This clearly confirms the superior performance of the bimetallic compositions. The most pronounced differences are observed at higher temperatures. At 500 °C, Pt(0.5%)/Ni(9.5%) delivers an impressive 90.1% $CH_4$ conversion, while Pt(1%)/Ni(9%) reaches 83.6%. The monometallic Ni(10%) and Pt(1%) catalysts show relatively moderate increases to 74.6% and 72.5%. However, the maximum catalytic performance is observed at higher temperatures (500–600 °C), where thermodynamic and kinetic limitations are further minimized. The maximum $H_2/CO$ ratio observed at 500 °C can be attributed to an optimal balance between methane decomposition and $CO_2$ activation. At this temperature, methane activation is sufficiently enhanced to generate hydrogen, while the reverse water-gas shift (RWGS) reaction ($CO_2 + H_2 \rightarrow CO + H_2O$) is not yet dominant. As a result, hydrogen production is relatively higher compared to CO formation, leading to an increased $H_2/CO$ ratio. At temperatures above 500 °C, the RWGS reaction becomes more significant, consuming hydrogen and producing additional CO, which reduces the $H_2/CO$ ratio. This explains the observed decline in the ratio at higher temperatures despite continued increases in overall conversion. At 550 °C, Pt(0.5%)/Ni(9.5%) reaches 92.4% and Pt(1%)/Ni(9%) climbs to 86.5%, whereas Ni(10%) and Pt(1%) provide 78.9% and 76.7% respectively. Finally, at the maximum temperature tested (600 °C), Pt(0.5%)/Ni(9.5%) catalyst achieves a peak $CH_4$ conversion of 95.7%, significantly higher than the 87.6% conversion of Pt(1%)/Ni(9%), while the Ni(10%) and Pt(1%) catalysts deliver 82.6% and 80.6% respectively. In summary, the bimetallic Pt/Ni catalysts consistently outperform the monometallic Ni and Pt catalysts across the entire temperature range, with the Pt(0.5%)/Ni(9.5%) composition demonstrating the highest activity. This enhanced performance is likely due to a synergistic interaction between Pt and Ni, which promotes greater $CH_4$ activation and reforming efficiency, especially at elevated temperatures.[64] From a catalytic standpoint, the appearance of the ~26–28° XRD feature and the correlated textural changes suggest stronger metal–support interaction (MSI) in Ni–Pt/KIT-5. MSI can stabilize smaller Ni domains and Ni–Pt alloyed sites against sintering (beneficial for activity and coking resistance), but also renders part of Ni harder to reduce (seen in TPR) and may lower the fraction of readily accessible metallic $Ni^0$ at low temperature. The performance trends we observe best activity/selectivity for 9%Ni–1%Pt, and slightly lower activity when Pt is increased or when porosity is more occluded, fit a balance between (i) alloying-enabled $CH_4$ activation and carbon removal, and (ii) MSI-driven stabilization *versus* over-anchoring. Thus, the new phase/signature near 26–28° is not just a crystallographic curiosity; it tracks a structure–property lever that helps explain both the SSA/SEM changes and the catalytic outcomes. The improved catalytic performance of Ni–Pt/KIT-5 catalysts can be directly correlated with the strong metal–support interaction and enhanced metal dispersion inferred from XRD and TPR analyses, which promote active $Ni^0$ site stabilization and suppress sintering and coke formation. The shift in reduction behavior (TPR), decrease in particle aggregation (TEM), and changes in textural properties (BET) collectively support the improved catalytic performance of bimetallic catalysts. The increase in $CH_4$ and $CO_2$ conversion with temperature is primarily due to the highly endothermic nature of the dry reforming reaction ($\Delta H > 0$), which is thermodynamically favored at higher temperatures. Elevated temperatures enhance the activation of stable $CH_4$ and $CO_2$ molecules, increasing reaction rates. In addition, higher temperatures improve the kinetics of surface reactions, including methane dissociation and $CO_2$ activation, leading to increased syngas production. At temperatures beyond 600 °C, the conversion may continue to increase; however, the extent of improvement depends on catalyst stability. While higher temperatures favor thermodynamics, excessive temperatures can lead to catalyst deactivation due to sintering of metal particles, loss of active surface area, and increased carbon formation through methane decomposition. In bimetallic Ni–Pt catalysts, improved resistance to sintering and coke formation helps maintain performance, but

prolonged operation at very high temperatures may still result in gradual activity decline.

The Fig. 8B shows a detailed comparison of $CO_2$ conversion efficiency for various KIT-5-supported catalysts under varying temperatures, specifically focusing on monometallic and bimetallic systems incorporating Ni and Pt. The study was conducted under the reaction conditions of 200 mg catalyst loading, a GHSV of 36 000 mL $g_{cat}^{-1}$ $h^{-1}$, and a $CH_4/CO_2/N_2$ feed ratio of 1 : 1 : 3. The temperature 300 °C, the $CO_2$ conversion starts relatively low across all catalysts. Pt(1%)-KIT-5 achieves 48.3%, while Ni(10%)-KIT-5 performs slightly better at 52%. The incorporation of both Pt and Ni significantly enhances the conversion rate, with Pt(0.5%)/Ni(9.5%)-KIT-5 showing a high 75.8%, and Pt(1%)/Ni(9%)-KIT-5 reaching 74%. As the temperature increases to 350 °C, a modest rise is seen: Pt-only catalyst improves to 53.3%, Ni-only to 55.6%, and the bimetallic catalysts exhibit conversion efficiencies of 77.6% and 74.7% respectively. Upon further temperature elevation to 400 °C, the conversion trends continue upward. The Pt(1%) catalyst reaches 58.6%, while Ni(10%) slightly outperforms it at 58.8%. The bimetallic Pt(0.5%)/Ni(9.5%) formulation leads again with 81.6%, followed by 75.9% for the Pt(1%)/Ni(9%) sample. At 450 °C, Ni(10%) gains more efficiency at 66.6%, surpassing Pt(1%) which climbs to 62.5%. The bimetallic catalysts improve further to 82.7% and 77.9%. At 500 °C, all catalysts show substantial increases: Pt(1%) reaches 68.7%, Ni(10%) at 71.3%, Pt(0.5%)/Ni(9.5%) at a remarkable 87.5%, and Pt(1%)/Ni(9%) at 80.8%. By 550 °C, the conversions become more distinguished: Pt-only catalyst records 71.4%, Ni-only catalyst rises to 74.7%, and the bimetallic systems reach 89.5% and 83.9%, respectively. At the highest tested temperature of 600 °C, performance peaks: Pt(1%) gives 74.5%, Ni(10%) climbs to 79.3%, Pt(0.5%)/Ni(9.5%) achieves the highest conversion at 92.7%, and Pt(1%)/Ni(9%) follows with 84.8%. In summary, the $CO_2$ conversion efficiency consistently improves with rising temperature across all catalysts. The bimetallic Pt–Ni formulations, particularly Pt(0.5%)/Ni(9.5%)-KIT-5, outperform both monometallic systems at every temperature point. This demonstrates a clear synergistic effect between Pt and Ni when supported on KIT-5, with optimal performance observed at higher operating temperatures.

The Fig. 8C illustrates the variation of the $H_2/CO$ molar ratio as a function of temperature during methane dry reforming using various supported catalysts—specifically, Ni-based and Pt-promoted Ni catalysts supported on mesoporous silica KIT-5. The catalytic performance was investigated with the same reaction parameters: 200 mg of catalyst, 36 000 mL $g^{-1}$ $h^{-1}$ GHSV, and a gas feed mix of $CH_4/CO_2/N_2$ = 1 : 1 : 3. The temperatures ranged from 300 °C to 600 °C. For the Pt(1%)-KIT-5 catalyst, the $H_2/CO$ ratio remained relatively stable across the temperature range. At 300 °C and 350 °C, the ratio was constant at 0.9, then gradually increased to 1.0 at 400 °C, 1.1 at 450 °C, remained 1.0 at 500 °C and 550 °C, and slightly rose to 1.2 at 600 °C. This trend indicates a limited ability of the monometallic Pt catalyst to enhance $H_2$ production, likely due to its low intrinsic methane activation capability.[65] The Ni(10%)-KIT-5 catalyst displayed a steady increase in the $H_2/CO$ ratio with rising temperature, beginning at 1.0 at 300 °C and 350 °C, increasing to 1.1 at 400 °C and 450 °C, reaching 1.4 at 500 °C, slightly decreasing to 1.2 at 550 °C and maintaining that value at 600 °C. This moderate performance reflects the typical activity of Ni catalysts, which are known for their effective $CH_4$ dissociation and moderate $CO_2$ activation. In contrast, the bimetallic catalysts showed significantly improved $H_2/CO$ ratios, suggesting synergistic interactions between Ni and Pt species. The Pt(0.5%)/Ni(9.5%)-KIT-5 catalyst showed a distinct advantage, with the ratio starting at 1.7 at 300 °C and 350 °C, further increasing to 1.8 at 400 °C, 1.9 at 450 °C, peaking at 2.2 at 550 °C, and then decreasing to 1.7 at 600 °C. This peak performance at intermediate temperature could indicate an optimal balance between methane and $CO_2$ conversions, possibly due to enhanced metal dispersion and reduced carbon deposition. Similarly, the Pt(1%)/Ni(9%)-KIT-5 catalyst also exhibited superior reforming efficiency compared to monometallic catalysts, although its $H_2/CO$ ratio was slightly lower than the 0.5% Pt-modified version. Starting at 1.4 at 300 °C, the ratio gradually increased to 1.5 between 350 °C and 450 °C, rose to 1.6 at 500 °C and remained consistent at 1.8 at 550 °C and then declined to 1.6 at 600 °C. The slightly reduced performance compared to the 0.5% Pt version could be attributed to Pt agglomeration at higher loadings, which may hinder Ni's activity by blocking active sites. Overall, the data reveals that bimetallic Ni–Pt catalysts significantly outperform their monometallic counterparts, particularly at mid-to-high temperatures, suggesting that fine-tuning the Pt-to-Ni ratio on mesoporous KIT-5 supports can optimize dry reforming activity and enhance syngas quality (*i.e.*, higher $H_2/CO$ ratios).[66,67]

### 4.1. Life time test

Various catalysts' catalytic activity Pt (1%). -KIT-5, Ni (10%) -Pt (0.5%)/Ni (9.5%), KIT-5 -Pt (1%), Ni (9%), and KIT-5 was analyzed on stream over time at 550 °C with a gas hourly space velocity (GHSV) of 36 000 mL $g_{cat}^{-1}$ $h^{-1}$ under reaction conditions of $CH_4/CO_2/N_2$ = 1 : 1 : 3. The primary metric used for comparison was methane ($CH_4$) conversion are shown in Fig. 9A. The monometallic Pt(1%)-KIT-5 catalyst displayed moderate catalytic activity, maintaining $CH_4$ conversion levels between 62.2% and 64.2% throughout the 8 hour test. It showed a relatively stable performance with only slight fluctuations, suggesting moderate activation of $CH_4$ under the given conditions. The Ni(10%)-KIT-5 catalyst also exhibited consistent $CH_4$ conversion, albeit slightly higher than that of Pt(1%)-KIT-5, ranging from 67.5% to 69.4%. This indicates that Ni, even without Pt, contributes significantly to $CH_4$ reforming activity, likely due to its known efficiency in activating methane molecules in dry reforming reactions. Its performance remains stable over time, suggesting good resistance to deactivation. Significantly improved activity was observed in the bimetallic catalysts. Pt(0.5%)/Ni(9.5%)-KIT-5 showed outstanding $CH_4$ conversion ranging from 92.3% to 94.2% over the 8 hour period. The conversion steadily increased, peaking at the 7th hour and maintaining above 93% afterward.[68] This synergy between Pt and Ni likely enhances the catalyst's ability to dissociate $CH_4$

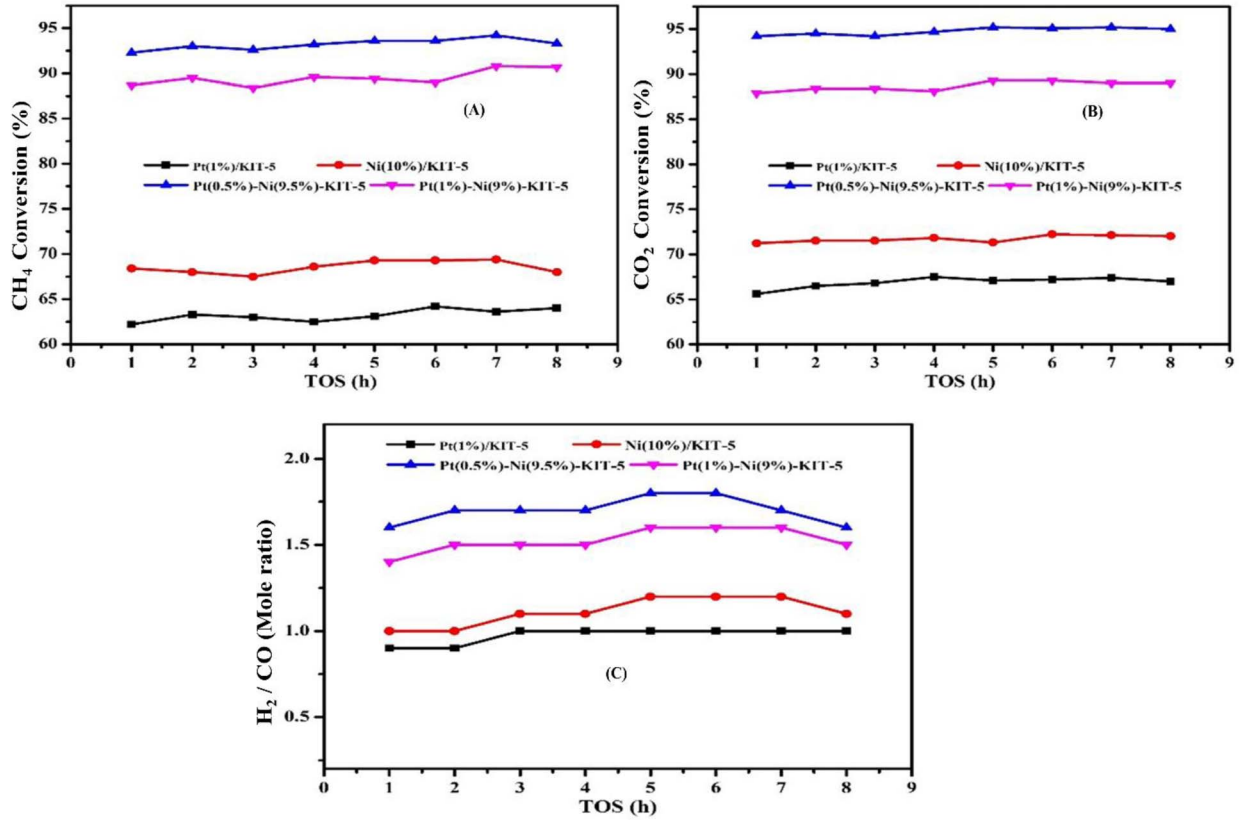


Fig. 9 Time on stream on the catalytic activity of Pt–Ni/KIT-5, and Pt–Ni/KIT-5 at 550 °C. (A) $CH_4$ conversion, (B) $CO_2$ conversion, and (C) $H_2$/CO ratio with reaction condition GHSV 36,000 mL $h^{-1}g_{cat}{}^{-1}$, $CH_4/CO_2$ 1 : 1 with $N_2$ at atmospheric pressure.

molecules more efficiently and reduce carbon deposition, resulting in superior stability and activity. Similarly, Pt(1%)/Ni(9%)-KIT-5 also demonstrated high catalytic activity, with $CH_4$ conversion rates ranging from 88.4% to 90.8%. While slightly lower than the Pt(0.5%)/Ni(9.5%) combination, it still significantly outperformed the monometallic variants. This suggests that increasing Pt beyond an optimal point does not proportionally enhance activity, possibly due to Pt particle agglomeration or blockage of active Ni sites. In conclusion, the bimetallic catalysts especially Pt(0.5%)/Ni(9.5%)-KIT-5 exhibited superior performance in $CH_4$ conversion, emphasizing the synergistic interaction between Pt and Ni *via* KIT-5 support. These findings emphasize the significance of metal contact and dispersion in improving the stability and catalytic efficiency of methane dry reforming.[69,70]

The catalytic activity of different catalysts Pt(1%)-KIT-5, Ni(10%)-KIT-5, Pt(0.5%)/Ni(9.5%)-KIT-5, and Pt(1%)/Ni(9%)-KIT-5 was compared under identical reaction conditions to assess their $CO_2$ conversion efficiency over time are shown in Fig. 9B. The trials were carried out utilizing a feed composition of $CH_4/CO_2/N_2$ in a 1 : 1 : 3 ratio, at a temperature of 550 °C and a GHSV of 36 000 mL $g^{-1}$ $h^{-1}$. Over the 8 hour time-on-stream (TOS) experiment, a clear trend in catalytic performance emerged, highlighting the superior behavior of bimetallic catalysts over monometallic ones.[71] Initially, the Pt(1%)-KIT-5 catalyst showed a modest $CO_2$ conversion rate of 65.6%, which gradually increased to 67.4% by the 7th hour, showing relatively stable yet limited activity. Similarly, the Ni(10%)-KIT-5 catalyst began at 71.2% conversion and showed a slight incremental rise to 72.2% by the 6th hour, indicating slightly better performance than the Pt-only system but still lacking robustness in activity growth. In contrast, the bimetallic Pt(0.5%)/Ni(9.5%)-KIT-5 catalyst consistently demonstrated the highest $CO_2$ conversion throughout the experiment. It started at a remarkable 94.2% conversion and peaked at 95.2% by the 5th and 7th hour, maintaining this level with negligible fluctuation indicative of excellent catalytic stability and synergy between Pt and Ni at optimal ratios. The second bimetallic catalyst, Pt(1%)/Ni(9%)-KIT-5, also outperformed the monometallic catalysts, starting at 87.9% and reaching a maximum of 89.3% during the 5th and 6th hour. While this formulation was slightly less active than the Pt(0.5%)/Ni(9.5%) variant, it still showed significant improvement over Pt or Ni alone, underscoring the critical role of Pt loading and metal dispersion in enhancing $CO_2$ reforming efficiency. Overall, the data underscore the superior catalytic performance of Pt–Ni bimetallic catalyst anchored on mesoporous KIT-5 structures, particularly when optimized at Pt(0.5%)/Ni(9.5%). This configuration not only achieved the highest and most stable $CO_2$ conversion rates but also exhibited outstanding durability under high-temperature conditions, suggesting its strong potential for industrial methane dry reforming applications.[72,73]

The data presented in Fig. 9C represents a detailed investigation into the catalytic activity over time of different metal-loaded KIT-5 catalysts namely Pt(1%)-KIT-5, Ni(10%)-KIT-5, Pt(0.5%)/Ni(9.5%)-KIT-5, and Pt(1%)/Ni(9%)-KIT-5 at 550 °C under specific reaction conditions ($H_2$/CO ratio, $CH_4/CO_2/N_2$ = 1 : 1 : 3, and GHSV = 36 000 mL $g^{-1}$ $h^{-1}$). The key focus of the study is to observe how catalytic performance evolves over a continuous 8 hour reaction stream. The monometallic Pt(1%)-KIT-5 catalyst exhibited relatively stable but low catalytic activity throughout the experiment, maintaining a steady value of 0.9 during the first two hours and increasing marginally to 1.0 from the third to the seventh hour. However, a slight decrease to 0.9 was noted in the final hour, possibly indicating a minor decline in catalytic stability. In contrast, the Ni(10%)-KIT-5 catalyst consistently demonstrated better activity than Pt(1%)-KIT-5. Activity began at 1.0 in the initial hour, grew steadily to 1.1 during the third, and stayed constant until the fourth hour. From the fifth to seventh hours, the activity rose to 1.2, before slightly declining to 1.1 in the final hour. This trend suggests that Ni-based catalysts possess superior intrinsic activity compared to Pt-only formulations, likely due to Ni's enhanced reforming capabilities in methane dry reforming reactions. A more notable improvement was observed with the bimetallic catalyst Pt(0.5%)/Ni(9.5%)-KIT-5. This catalyst began with an activity of 1.6 in the first hour, significantly higher than either monometallic catalyst. Its activity gradually increased to 1.7 between hours two and four, then rose further to 1.8 during the fifth and sixth hours. Although a slight drop to 1.7 and 1.6 was observed in the seventh and eighth hours, respectively, the overall trend indicates enhanced and sustained catalytic performance. The synergy between Pt and Ni in this composition seems to promote both methane activation and $CO_2$ reforming, possibly due to the improved dispersion of active sites and increased resistance to coking. The catalyst with the highest platinum content among the bimetallic samples, Pt(1%)/Ni(9%)-KIT-5, delivered the best catalytic performance over the entire time stream. The activity grew progressively from an amazing 1.4 in the beginning hour to 1.5 in the second, and remained at that pace until the fourth hour. It then peaked at 1.6 from the fifth to seventh hours, showing no decline until the eighth hour where it slightly reduced to 1.5. This sustained high performance suggests a significant promotional effect of higher Pt loading in combination with Ni, likely facilitating better metal–support interaction, enhanced reducibility, and resistance to deactivation under high-temperature reforming conditions. Finally, the findings clearly show that during methane dry reforming, bimetallic catalysts especially those with optimal Pt/Ni ratios, perform better than their monometallic counterparts with regard to of both catalytic efficiency and temporal stability. The crucial function that Pt plays in altering

Table 3 Systematic comparison of supported Ni–Pt catalysts for syngas production *via* DRM

| S. no | Catalyst | Support | Ni loading (wt%) | Preparation method | Reaction temp (°C) | $CH_4$ conv. (%) | $CO_2$ conv. (%) | $H_2$/CO ratio | Coke resistance | Ref. |
|---|---|---|---|---|---|---|---|---|---|---|
| 1 | $Ni/Al_2O_3$ | γ-Alumina | 10 | Wet impregnation | 800 | 78 | 75 | ∼1.0 | Moderate coke deposition | 76 |
| 2 | $Ni/MgAl_2O_4$ | Spinel | 10 | Co-precipitation | 750 | 82 | 79 | 0.95 | Improved coke resistance | 78 |
| 3 | $Ni/SiO_2$ | Silica | 10 | Dry impregnation | 800 | 70 | 68 | 0.98 | High coke formation | 79 |
| 4 | $Ni/CeO_2$ | Ceria | 10 | Wet impregnation | 750 | 85 | 83 | ∼1.1 | Excellent resistance | 80 |
| 5 | $Ni/ZrO_2$ | Zirconia | 10 | Sol–gel method | 750 | 87 | 84 | 1.0 | Low coke accumulation | 81 |
| 6 | $Ni/TiO_2$ | Titania | 10 | Wet impregnation | 750 | 75 | 73 | ∼1.0 | Moderate | 82 |
| 7 | Ni/MgO | Magnesium oxide | 10 | Co-precipitation | 800 | 88 | 85 | 0.98 | Excellent | 83 |
| 8 | Ni/KIT-6 | Mesoporous silica | 5 | Incipient wetness | 700 | 80 | 77 | ∼0.9 | Moderate | 84 |
| 9 | $Ni–SrTiO_3$ | Perovskite | 10 | Sol–gel | 800 | 89 | 87 | ∼1.0 | High resistance | 85 |
| 10 | Ni–Co/KCC-1 | Fibrous silica | 9%Ni–1%Co | Wet impregnation | 800 | 92 | 90 | 0.88 | Excellent resistance | 86 |
| 11 | $Ni–La_2O_3–Al_2O_3$ | Mixed oxide | 10 | Sol–gel | 750 | 85 | 82 | ∼1.0 | Good | 87 |
| 12 | $Ni/Ce–ZrO_2$ | Ceria–zirconia | 10 | Impregnation | 750 | 90 | 88 | ∼1.1 | Very high | 88 |
| 13 | Ni/SBA-15 | Mesoporous silica | 5 | Incipient wetness | 700 | 76 | 73 | 0.95 | Moderate | 89 |
| 14 | Ni/MCM-41 | Mesoporous silica | 5 | Incipient wetness | 700 | 74 | 70 | ∼0.9 | Moderate | 90 |
| **15** | **Ni–Pt-KIT-5** | **Silica** | **9%** | **Wet impregnation** | **550** | **95** | **88.5** | **1 : 1** | **Low coke accumulation** | **This work** |

the catalytic surface and fostering long-term efficiency is highlighted by the better performance of Pt(1%)/Ni(9%)-KIT-5.[74,75]

### 4.2. Comparative studies

The data from the Table 3 provides a comprehensive comparison of various supported Ni and Ni–Pt catalysts used for syngas synthesis *via* the DRM. Each catalyst exhibits different performance metrics based on its support material, preparation method, and operating temperature. The traditional $Ni/Al_2O_3$ catalyst with 10 wt% Ni prepared *via* wet impregnation at 800 °C shows moderate methane and $CO_2$ conversions (78% and 75%, respectively) with a $H_2/CO$ ratio close to 1.0, but suffers from moderate coke deposition. In contrast, $Ni/MgAl_2O_4$ prepared by co-precipitation at 750 °C achieves slightly better conversions (82% $CH_4$ and 79% $CO_2$) and exhibits improved resistance to coke formation. The $Ni/SiO_2$ catalyst, despite having similar Ni loading and operating temperature, shows lower conversions (70% $CH_4$ and 68% $CO_2$) and is prone to high coke formation. $Ni/CeO_2$ and $Ni/ZrO_2$ catalysts both display superior performance, with conversions above 85% and excellent to low coke resistance. Particularly, $Ni/ZrO_2$ prepared *via* the sol–gel method at 750 °C yields 87% $CH_4$ and 84% $CO_2$ conversion with a $H_2/CO$ ratio of 1.0. $Ni/TiO_2$, while achieving reasonable conversions (75% $CH_4$ and 73% $CO_2$), only shows moderate coke resistance. Ni/MgO stands out with high conversions (88% $CH_4$ and 85% $CO_2$) and excellent coke resistance at 800 °C. Among mesoporous silica-based supports, Ni/KIT-6, Ni/SBA-15, and Ni/MCM-41 (all at 5 wt% Ni) demonstrate moderate conversions (76–80% $CH_4$ and 70–77% $CO_2$) with relatively low $H_2/CO$ ratios and moderate coke resistance. The perovskite-supported Ni–$SrTiO_3$ and mixed oxide-supported Ni–$La_2O_3$–$Al_2O_3$ catalysts also perform well, with conversions exceeding 85% and high coke resistance. Ni/Ce–$ZrO_2$ catalyst prepared by impregnation at 750 °C displays remarkable conversions of 90% for $CH_4$ and 88% for $CO_2$, along with a very high coke resistance. Finally, at a lesser process temperature of 550 °C, the Ni–Pt/KIT-5 catalyst created in this work, including 9 weight percent Ni, exhibits exceptional performance. It attains the maximum $CH_4$ conversion of 95% and a $CO_2$ conversion of 88.5%, with a $H_2/CO$ ratio of 1 : 1 and low coke accumulation, indicating the synergistic effect of the bimetallic system and the mesoporous silica support.[77]

### 4.3. Mechanism study

Understanding the reaction mechanism of dry catalytic reforming of methane (DRM) is crucial for identifying the elementary steps involved and developing effective strategies to enhance catalyst stability and prevent deactivation. The DRM pathway is greatly influenced by the nature of the catalyst and its surface chemistry are depicted in Fig. 10. In the Pt–Ni/KIT-5 catalyst case, the reaction initiates with the adsorption of $CH_4$ and $CO_2$ molecules onto the catalyst's surface. Platinum, incorporated as a promoter, enhances the dissociative adsorption of $CO_2$, resulting in the formation of carbon monoxide and reactive surface oxygen species. Simultaneously, methane undergoes activation primarily at the nickel sites, where it is

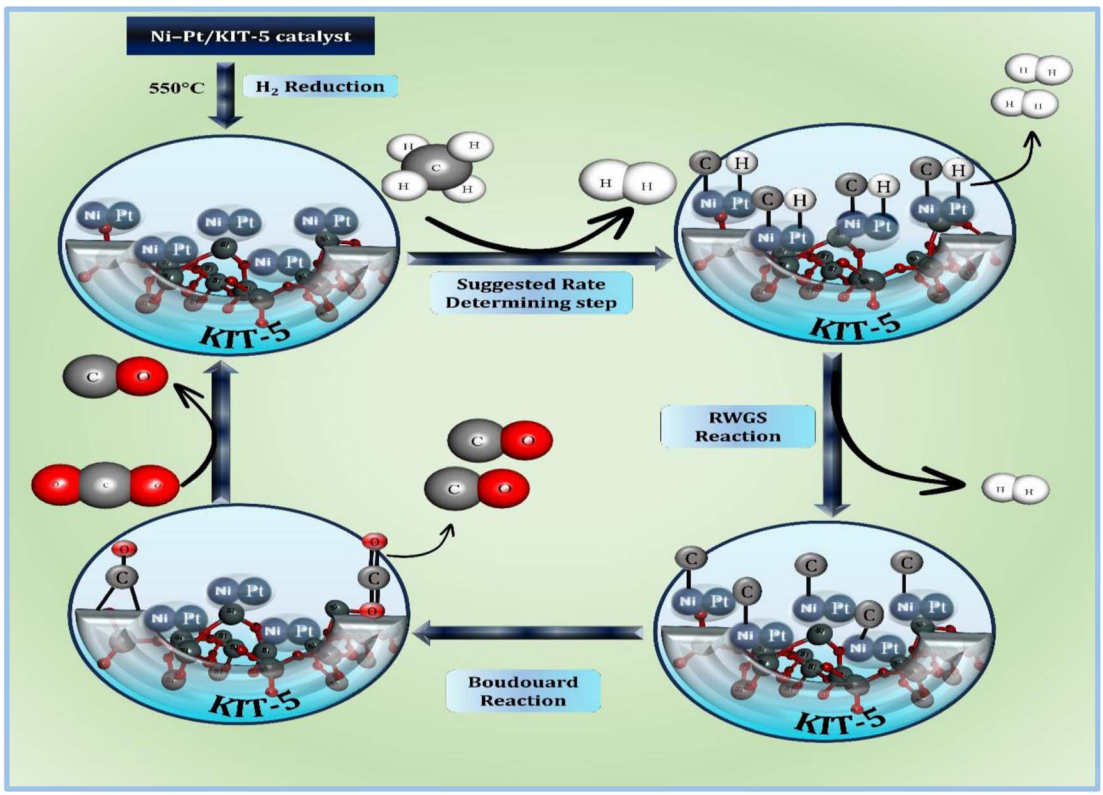


Fig. 10 Proposed reaction pathway for methane dry reforming on Pt–Ni/KIT-5.

cleaved to generate $CH_x$ fragments (where $x = 1$–3) and hydrogen atoms. As the reaction progresses, various surface intermediates such as monodentate and bidentate carbonate species, as well as linear carbonyl groups, are formed. These intermediates play a significant role in the removal of carbonaceous deposits by facilitating their oxidation. The reactive oxygen species derived from $CO_2$ dissociation contribute to the continuous cleaning of the catalyst surface by oxidizing carbon residues, thus suppressing coke formation. The hydrogen atoms generated from methane decomposition eventually combine to form molecular hydrogen ($H_2$), contributing to the syngas ($H_2$ and CO) output. Methane undergoes stepwise dehydrogenation forming $CH_x$ intermediates ($CH_4 \rightarrow CH_3^* \rightarrow CH_2^* \rightarrow CH^* \rightarrow C^*$), while $CO_2$ is activated through dissociative adsorption to produce CO* and O* species on the catalyst surface. These reaction pathways are consistent with established DRM mechanisms reported for Ni-based catalysts.[36,37] The presence of Pt enhances hydrogen spillover and facilitates the reduction of Ni species, improving catalytic activity and coke resistance, as reported in previous studies.[21,38] This intricate mechanism underscores the synergistic interaction between Pt and Ni in improving both the activity and durability of the Pt–Ni/KIT-5 catalyst during the DRM process. The proposed mechanism is therefore consistent with well-established models such as Langmuir–Hinshelwood and Eley–Rideal pathways reported in the literature.[25]

## 5. Conclusions

In this work, bimetallic Ni–Pt catalysts supported on KIT-5 were synthesized and evaluated for their performance in the dry reforming of methane (DRM) to produce syngas. These bimetallic systems outperformed their monometallic counterparts, showing significantly improved catalytic activity. The interaction between Ni and Pt facilitates the development of $NiPtO_2$ spinel-like phases, which effectively inhibited the sintering and aggregation of nickel particles. The improved catalytic performance of Ni–Pt/KIT-5 catalysts is attributed to enhanced metal dispersion and modified reducibility arising from Ni–Pt interaction, as supported by TPR, BET, and TEM analyses, rather than definitive evidence of new crystalline phase formation. Analysis of both fresh and used catalysts indicated that the compositions 9.5%Ni–0.5%Pt and 9%Ni–1%Pt were particularly effective in suppressing the formation of graphitic carbon and demonstrated strong resistance to carbon deposition. Among the tested catalysts, 9.5%Ni–0.5%Pt/KIT-5 delivered the highest conversion rates for methane and carbon dioxide, along with increased syngas production. A weak reflection at $2\theta \approx 26$–28° in Ni–Pt samples indicating that the enhanced catalytic performance is primarily governed by strong metal–support interaction and improved dispersion of active species, rather than the formation of distinct new crystalline phases, correlates with reduced SSA and the rounded particle morphology, indicating strengthened MSI that contributes to sintering resistance and sustained DRM activity. The strong metal–support interactions found in the Ni–Pt/KIT-5 catalysts serve as the reason for their improved stability and performance. Cooperative effects between the metals, the presence of thermally stable $PtO_2$ domains, and the open fibrous framework of KIT-5 enhance reactant accessibility. The temperature-dependent increase in catalytic performance is consistent with the endothermic nature of DRM, although catalyst stability at temperatures above 600 °C remains an important consideration. The XRD/TPR trends are consistent with stronger Ni–Pt interaction and the possible formation of Ni–Pt interfacial oxide domains, although no direct crystallographic evidence for a discrete Ni–Pt oxide phase was obtained in this study. The catalyst also retained its activity for more than 8 hours of continuous DRM operation without noticeable deactivation, demonstrating its promise for long-term applications.

## Conflicts of interest

The authors declare no conflicts of interest.

## Data availability

Data supporting this study are included within the article. No supplementary data, software, or code are associated with this work.

## Acknowledgements

The authors extend their appreciation to the Deanship of Research and Graduate Studies at King Khalid University for funding this work through Large Research Project under grant number RGP2/316/46. This work was supported by the Princess Nourah bint Abdulrahman University Researchers Supporting Project number (PNURSP2026R584), Princess Nourah bint Abdulrahman University, Riyadh, Saudi Arabia.

## References

1 A. S. Al-Fatesh, J. K. Abu-Dahrieh, H. Atia, U. Armbruster, A. A. Ibrahim, W. U. Khan, *et al.*, Effect of pre-treatment and calcination temperature on $Al_2O_3$-$ZrO_2$ supported Ni-Co catalysts for dry reforming of methane, *Int. J. Hydrogen Energy*, 2019, **44**, 21546–21558, DOI: 10.1016/j.ijhydene.2019.06.085.

2 A. S. Farooqi, M. Yusuf, N. A. Mohd Zabidi, R. Saidur, K. Sanaullah, A. S. Farooqi, *et al.*, A comprehensive review on improving the production of rich-hydrogen via combined steam and $CO_2$ reforming of methaneover Ni-based catalysts, *Int. J. Hydrogen Energy*, 2021, **46**, 31024–31040, DOI: 10.1016/j.ijhydene.2021.01.049.

3 M. Aguiar, B. B. Cazula, L. M. Saragiotto Colpini, C. E. Borba, F. Alves da Silva, F. B. Noronha, *et al.*, Si-MCM-41 obtained from different sources of silica and its application as support for nickel catalysts used in dry reforming of methane, *Int. J. Hydrogen Energy*, 2019, **44**, 32003–32018, DOI: 10.1016/j.ijhydene.2019.10.118.

4 N. Wang, X. Yu, K. Shen, W. Chu and W. Qian, Synthesis, characterization and catalytic performance of MgO-coated Ni/SBA-15 catalysts for methane dry reforming to syngas

and hydrogen, *Int. J. Hydrogen Energy*, 2013, **38**, 9718–9731, DOI: 10.1016/j.ijhydene.2013.05.097.

5 K. Wittich, M. Kr€amer, N. Bottke and S. A. Schunk, Catalytic dry reforming of methane: insights from model systems, *ChemCatChem*, 2020, **12**, 2130–2147, DOI: 10.1002/cctc.201902142.

6 F. Sharifianjazi, A. Esmaeilkhanian, L. Bazli, S. Eskandarinezhad, S. Khaksar, P. Shafiee, *et al.*, A review on recent advances in dry reforming of methane over Ni- and Co-based nanocatalysts, *Int. J. Hydrogen Energy*, 2021, **47**(100), 42213–42233, DOI: 10.1016/j.ijhydene.2021.11.172.

7 P. G. Lustemberg, P. J. Ramírez, Z. Liu, R. A. Gutierrez, D. G. Grinter, J. Carrasco, *et al.*, Room-temperature activation of methane and dry Re-forming with $CO_2$ on Ni-$CeO_2$(111) surfaces: effect of $Ce_{3+}$ sites and metal-support interactions on C-H bond cleavage, *ACS Catal.*, 2016, **6**, 8184–8191, DOI: 10.1021/acscatal.6b02360.

8 L. Tang, X. Huang, J. Ran, F. Guo, J. Niu, H. Qiu, *et al.*, Density functional theory studies on direct and oxygen assisted activation of CeH bond for dry reforming of methane over RheNi catalyst, *Int. J. Hydrogen Energy*, 2022, **47**, 30391–30403, DOI: 10.1016/j.ijhydene.2022.07.002.

9 T. Roussiere, L. Schulz, K. M. Schelkle, G. Wasserschaff, A. Milanov, E. Schwab, *et al.*, Structure-activity relationships of nickel-hexaaluminates in reforming reactions Part II: activity and stability of nanostructured nickel- hexaaluminate-based catalysts in the dry reforming of methane, *ChemCatChem*, 2014, **6**, 1447–1452, DOI: 10.1002/cctc.201300958.

10 O. Mohan, L. A. A. Shambhawi and S. H. Mushrif, Investigating methane dry reforming on Ni and B promoted Ni surfaces: DFT assisted microkinetic analysis and addressing the coking problem, *Catal. Sci. Technol.*, 2020, **10**, 6628–6643, DOI: 10.1039/d0cy00939c.

11 J. Wei and E. Iglesia, Reaction pathways and site requirements for the activation and chemical conversion of methane on Ru based catalysts, *J. Phys. Chem. B*, 2004, **108**, 7253–7262, DOI: 10.1021/jp030783l.

12 J. Wei and E. Iglesia, Isotopic and kinetic assessment of the mechanism of reactions of CH 4 with $CO_2$ or $H_2O$ to form synthesis gas and carbon on nickel catalysts, *J. Catal.*, 2004, **224**, 370–383, DOI: 10.1016/j.jcat.2004.02.032.

13 A. S. Al-Fatesh, R. Kumar, A. H. Fakeeha, S. O. Kasim, J. Khatri, A. A. Ibrahim, *et al.*, Promotional effect of magnesium oxide for a stable nickel-based catalyst in dry reforming of methane, *Sci. Rep.*, 2020, **10**, 1–10, DOI: 10.1038/s41598-02070930-1.

14 S. Arora and R. Prasad, An overview on dry reforming of methane: strategies to reduce carbonaceous deactivation of catalysts, *RSC Adv.*, 2016, **6**, 108668–108688, DOI: 10.1039/c6ra20450c.

15 A. Giehr, L. Maier, S. A. Schunk and O. Deutschmann, Thermodynamic considerations on the oxidation state of Co/g-Al2O3 and Ni/g-Al2O3 catalysts under dry and steam reforming conditions, *ChemCatChem*, 2018, **10**, 751–757, DOI: 10.1002/cctc.201701376.

16 J. Titus, T. Roussiere, G. Wasserschaff, S. Schunk, A. Milanov, E. Schwab, *et al.*, Dry reforming of methane with carbon dioxide over NiO-MgO-ZrO2, *Catal. Today*, 2016, **270**, 68–75, DOI: 10.1016/j.cattod.2015.09.027.

17 Z. Zuo, S. Liu, Z. Wang, C. Liu, W. Huang, J. Huang, *et al.*, Dry reforming of methane on single-site Ni/MgO catalysts: importance of site confinement, *ACS Catal.*, 2018, **8**, 9821–9835, DOI: 10.1021/acscatal.8b02277.

18 F. Morales Anzures, P. Salinas Hernandez, G. Mondragon Galicia, A. Gutierrez Martínez, F. Tzompantzi Morales, M. A. Romero Romo, *et al.*, Synthetic gas production by dry reforming of methane over Ni/$Al_2O_3$eZr$O_2$ catalysts: high $H_2$/CO ratio, *Int. J. Hydrogen Energy*, 2021, **46**, 26224–26233, DOI: 10.1016/j.ijhydene.2021.05.073.

19 J. Zhang and F. Li, Coke-resistant Ni at $SiO_2$ catalyst for dry reforming of methane, *Appl. Catal., B*, 2015, **176–177**, 513–521, DOI: 10.1016/j.apcatb.2015.04.039.

20 X. Li, D. Li, H. Tian, L. Zeng, Z. J. Zhao and J. Gong, Dry reforming of methane over Ni/$La_2O_3$ nanorod catalysts with stabilized Ni nanoparticles, *Appl. Catal., B*, 2017, **202**, 683–694, DOI: 10.1016/j.apcatb.2016.09.071.

21 R. O. da Fonseca, R. C. Rabelo-Neto, R. C. C. Sim∼ oes, L. V. Mattos and F. B. Noronha, Pt supported on doped $CeO_2$/$Al_2O_3$ as catalyst for dry reforming of methane, *Int. J. Hydrogen Energy*, 2020, **45**, 5182–5191, DOI: 10.1016/j.ijhydene.2019.09.207.

22 Y. Lou, M. Steib, Q. Zhang, K. Tiefenbacher, A. Horvath, A. Jentys, *et al.*, Design of stable Ni/$ZrO_2$ catalysts for dry reforming of methane, *J. Catal.*, 2017, **356**, 147–156, DOI: 10.1016/j.jcat.2017.10.009.

23 B. Li, X. Yuan, L. Li, B. Li, X. Wang and K. Tomishige, Lanthanide oxide modified nickel supported on mesoporous silica catalysts for dry reforming of methane, *Int. J. Hydrogen Energy*, 2021, **46**, 31608–31622, DOI: 10.1016/j.ijhydene.2021.07.056.

24 B. C. Ekeoma, M. Yusuf, K. Johari and B. Abdullah, Mesoporous silica supported Ni-based catalysts for methane dry reforming: a review of recent studies, *Int. J. Hydrogen Energy*, 2022, DOI: 10.1016/j.ijhydene.2022.05.297.

25 A. S. Al-fatesh, R. Kumar, S. O. Kasim, A. A. Ibrahim, A. H. Fakeeha and A. E. Abasaeed, Efect of cerium promoters on an MCM 41-supported nickel catalyst in dry reforming of methane, *Ind. Eng. Chem. Res.*, 2022, **61**(1), 164–174, DOI: 10.1021/acs.iecr.1c03163.

26 W. Yang, H. Liu, Y. Li, H. Wu and D. He, $CO_2$ reforming of methane to syngas over highly-stable Ni/SBA-15 catalysts prepared by P123-assisted method, *Int. J. Hydrogen Energy*, 2016, **41**, 1513–1523, DOI: 10.1016/j.ijhydene.2015.11.044.

27 Z. Taherian, A. Khataee and Y. Orooji, Nickel-based nanocatalysts promoted over MgO-modified SBA-16 for dry reforming of methane for syngas production: impact of support and promoters, *J. Energy Inst.*, 2021, **97**, 100–108, DOI: 10.1016/j.joei.2021.04.005.

28 S. Kweon, Y. W. Kim, C. H. Shin, M. B. Park and H. K. Min, Nickel silicate beta zeolite prepared by interzeolite transformation: a highly active and stable catalyst for dry

reforming of methane, *Chem. Eng. J.*, 2022, **431**, 133364, DOI: 10.1016/j.cej.2021.133364.
29 F. Gholizadeh, A. Izadbakhsh, J. Huang and Y. Zi-Feng, Catalytic performance of cubic ordered mesoporous alumina supported nickel catalysts in dry reforming of methane, *Microporous Mesoporous Mater.*, 2021, **310**, 110616, DOI: 10.1016/j.micromeso.2020.110616.
30 C. C. Chong, Y. W. Cheng, M. B. Bahari, L. P. Teh, S. Z. Abidin and H. D. Setiabudi, Development of nanosilica-based catalyst for syngas production via $CO_2$ reforming of $CH_4$: a review, *Int. J. Hydrogen Energy*, 2021, **46**, 24687–24708, DOI: 10.1016/j.ijhydene.2020.01.086.
31 E. Febriyanti, V. Suendo, R. R. Mukti, A. Prasetyo, A. F. Arifin, M. A. Akbar, *et al.*, Further insight into the definite morphology and formation mechanism of mesoporous silica KCC-1, *Langmuir*, 2016, **32**, 5802–5811, DOI: 10.1021/acs.langmuir.6b00675.
32 A. A. Abdulrasheed, A. A. Jalil, M. Y. S. Hamid, T. J. Siang and T. A. T. Abdullah, Dry reforming of CH4 over stabilized NiLa@KCC-1 catalyst: effects of la promoter and optimization studies using RSM, *J. CO2 Util.*, 2020, **37**, 230–239, DOI: 10.1016/j.jcou.2019.12.018.
33 T. J. Siang, A. A. Jalil, H. U. Hambali, A. A. Abdulrasheedand and M. S. Azami, Dendritic mesoporous Ni/KCC-1 for partial oxidation of methane to syngas, *IOP Conf. Ser.: Mater. Sci. Eng.*, 2020, **808**, 012006, DOI: 10.1088/1757-899X/808/1/012006.
34 N. A. K. Aramouni, J. Zeaiter, W. Kwapinski, J. J. Leahy and M. N. Ahmad, Eclectic trimetallic NieCoeRu catalyst for the dry reforming of methane, *Int. J. Hydrogen Energy*, 2020, **45**, 17153–17163, DOI: 10.1016/j.ijhydene.2020.04.261.
35 M. Cichy, M. Panczyk, G. Słowik, W. Zawadzki and T. Borowiecki, NieRe alloy catalysts on $Al_2O_3$ for methane dry reforming, *Int. J. Hydrogen Energy*, 2022, **47**, 16528–16543, DOI: 10.1016/j.ijhydene.2022.03.147.
36 S. Das, M. Sengupta, A. Bag, M. Shah and A. Bordoloi, Facile synthesis of highly disperse Ni-Co nanoparticles over mesoporous silica for enhanced methane dry reforming, *Nanoscale*, 2018, **10**, 6409–6425, DOI: 10.1039/c7nr09625a.
37 M. Ocsachoque, F. Pompeo and G. Gonzalez, Rh-Ni/$CeO_2$-$Al_2O_3$ catalysts for methane dry reforming, *Catal. Today*, 2011, **172**, 226–231, DOI: 10.1016/j.cattod.2011.02.057.
38 D. G. Araiza, D. G. Arcos, A. Gomez-Cortes and G. Díaz, Dry reforming of methane over Pt-Ni/$CeO_2$ catalysts: effect of the metal composition on the stability, *Catal. Today*, 2021, **360**, 46–54, DOI: 10.1016/j.cattod.2019.06.018.
39 R. K. Singha, A. Shukla, A. Sandupatla, G. Deo and R. Bal, Synthesis and catalytic activity of a Pd doped Ni-MgO catalyst for dry reforming of methane, *J. Mater. Chem.*, 2017, **5**, 15688–15699, DOI: 10.1039/c7ta04452f.
40 A. Alvarez Moreno, T. Ramirez-Reina, S. Ivanova, A. C. Roger, M. A. Centeno and J. A. Odriozola, Bimetallic NieRu and NieRe catalysts for dry reforming of methane: understanding the synergies of the selected promoters, *Front. Chem.*, 2021, **9**, 1–10, DOI: 10.3389/fchem.2021.694976.
41 X. Duan, J. Pan, X. Yang, C. Wan, X. Lin, D. Li, *et al.*, Nickel cobalt bimetallic catalysts prepared from hydrotalcite like compounds for dry reforming of methane, *Int. J. Hydrogen Energy*, 2022, DOI: 10.1016/j.ijhydene.2022.05.211.
42 Z. Liu, F. Zhang, N. Rui, X. Li, L. Lin, L. E. Betancourt, *et al.*, Highly active ceria-supported Ru catalyst for the dry reforming of methane: in situ identification of Rud+-Ce3+ interactions for enhanced conversion, *ACS Catal.*, 2019, **9**, 3349–3359, DOI: 10.1021/acscatal.8b05162.
43 N. A. A. Fatah, A. A. Jalil, S. Triwahyono, N. Yusof, C. R. Mamat, S. M. Izan, *et al.*, Favored hydrogenation of linear carbon monoxide over cobalt loaded on fibrous silica KCC-1, *Int. J. Hydrogen Energy*, 2020, **45**, 9522–9534, DOI: 10.1016/j.ijhydene.2020.01.144.
44 M. Xiong, X. Wang, S. Ji, Y. Liu, H. Zhao, Z. Gong and D. Zhang, A Tetranuclear Thorium-Containing Hexameric Antimonotungstate: Synthesis, Structure, and Catalysis of the Knoevenagel Condensation, *Inorg. Chem.*, 2026, **65**(12), 6802–6810, DOI: 10.1021/acs.inorgchem.6c00156.
45 A. Fihri, M. Bouhrara, U. Patil, D. Cha, Y. Saih and V. Polshettiwar, Fibrous nano-silica supported ruthenium (KCC-1/Ru): a sustainable catalyst for the hydrogenolysis of alkanes with good catalytic activity and lifetime, *ACS Catal.*, 2012, **2**, 1425–1431, DOI: 10.1021/cs300179q.
46 J. Guerrero-Caballero, T. Kane, N. Haidar, L. Jalowiecki Duhamel and A. L∈ofberg, Ni, Co, Fe supported on Ceria and Zr doped Ceria as oxygen carriers for chemical looping dry reforming of methane, *Catal. Today*, 2019, **333**, 251–258, DOI: 10.1016/j.cattod.2018.11.064.
47 P. Gautam, M. Dhiman, V. Polshettiwar and B. M. Bhanage, KCC-1 supported palladium nanoparticles as an efficient and sustainable nanocatalyst for carbonylative Suzuki-Miyaura cross-coupling, *Green Chem.*, 2016, **18**, 5890–5899, DOI: 10.1039/c6gc02012g.
48 R. Sadek, K. A. Chalupka, P. Mierczynski, W. Maniukiewicz, J. Rynkowski, J. Gurgul, *et al.*, The catalytic performance of NiCo/Beta zeolite catalysts in Fischer-Tropsch synthesis, *Catalysts*, 2020, **10**, 112, DOI: 10.3390/catal10010112.
49 H. S. Oboudatian and J. Safaei-Ghomi, Silica nanospheres KCC-1 as a good catalyst for the preparation of 2-amino-4H chromenes by ultrasonic irradiation, *Sci. Rep.*, 2022, **12**, 1–15, DOI: 10.1038/s41598-022-05993-3.
50 H. Guan, C. Shao, S. Wen, B. Chen, J. Gong and X. Yang, A novel method for preparing $Co_3O_4$ nanofibers by using electrospun PVA/cobalt acetate composite fibers as precursor, *Mater. Chem. Phys.*, 2003, **82**, 1002–1006, DOI: 10.1016/j.matchemphys.2003.09.003.
51 J. Dou, Y. Tang, L. Nie, C. M. Andolina, X. Zhang, S. House, *et al.*, Complete oxidation of methane on $Co_3O_4$/$CeO_2$ nanocomposite: a synergic effect, *Catal. Today*, 2018, **311**, 48–55, DOI: 10.1016/j.cattod.2017.12.027.
52 E. Umeshbabu, G. Rajeshkhanna, P. Justin and G. R. Rao, NiCo2O4/rGO hybrid nanostructures for efficient electrocatalytic oxygen evolution, *J. Solid State Electrochem.*, 2016, **20**, 2725–2736, DOI: 10.1007/s10008-016-3278-4.
53 M. Zhang, M. Zhao, R. Chen, J. Liu, Q. Liu, J. Yu, *et al.*, Fabrication of the pod-like KCC-1/$TiO_2$ superhydrophobic

surface on AZ31 Mg alloy with stability and photocatalytic property, *Appl. Surf. Sci.*, 2020, **499**, 143933, DOI: 10.1016/j.apsusc.2019.143933.

54 J. Liu, Q. Zhang, C. Chen, *et al.*, Tuning Lewis acid in nickel-containing polyoxometalates for enhanced ethanol selectivity of methane electrooxidation reactions, *Nano Res.*, 2026, **19**, 94908604, DOI: 10.26599/NR.2026.94908604.

55 J. Liu, Q. Zhang, S. Zhang, C. Chen, J. Jiang, Y. Luo and J. Xu, Nitrogen-doped carbon layer thickness modulates the Cu0/Cu+ interface for selective and stable CO2 electroreduction to ethylene, *Chem. Commun.*, 2026, **62**, 8733–8737, DOI: 10.1039/D6CC00135A.

56 G. Tian, X. Liu, C. Zhang, *et al.*, Accelerating syngas-to-aromatic conversion via spontaneously monodispersed Fe in ZnCr2O4 spinel, *Nat. Commun.*, 2022, **13**, 5567, DOI: 10.1038/s41467-022-33217-9.

57 S. Damyanova, B. Pawelec, K. Arishtirova and J. L. G. Fierro, Ni-based catalysts for reforming of methane with CO2, *Int. J. Hydrogen Energy*, 2012, **37**, 15966–15975, DOI: 10.1016/j.ijhydene.2012.08.056.

58 Z. Boukha, M. Kacimi, M. F. R. Pereira, J. L. Faria, J. L. Figueiredo and M. Ziyad, Methane dry reforming on Ni loaded hydroxyapatite and fluoroapatite, *Appl. Catal., A*, 2007, **317**, 299–309, DOI: 10.1016/j.apcata.2006.10.029.

59 A. A. Abdulrasheed, A. A. Jalil, M. Y. S. Hamid, T. J. Siang, N. A. A. Fatah, S. M. Izan, *et al.*, Dry reforming of methane to hydrogen-rich syngas over robust fibrous KCC-1 stabilized nickel catalyst with high activity and coke resistance, *Int. J. Hydrogen Energy*, 2020, **45**, 18549–18561, DOI: 10.1016/j.ijhydene.2019.04.126.

60 Q. Hu, H. Lou, Z. Niu, J. Zhang, X. Wang, H. Jin and C. Ye, A combined experimental and simulation study on toluene cracking: synergistic strategy of Ni loading, alkali treatment, and atmosphere activation on HZSM-5 zeolite, *J. Energy Inst.*, 2026, **125**, 102467, DOI: 10.1016/j.joei.2026.102467.

61 G. Tyuliev and S. Angelov, The nature of excess oxygen in Co3O4+ε, *Appl. Surf. Sci.*, 1988, **32**, 381–391, DOI: 10.1016/0169-4332(88)90089-X.

62 T. C. Chang, Y. T. Lu, C. H. Lee, J. K. Gupta, L. J. Hardwick, C. C. Hu, *et al.*, The effect of degrees of inversion on the electronic structure of spinel NiCo2O4: a density functional theory study, *ACS Omega*, 2021, **6**, 9692–9699, DOI: 10.1021/acsomega.1c00295.

63 T. H. Lim, S. J. Cho, H. S. Yang, M. H. Engelhard and D. H. Kim, Effect of Co/Ni ratios in cobalt nickel mixed oxide catalysts on methane combustion, *Appl. Catal., A*, 2015, **505**, 62–69, DOI: 10.1016/j.apcata.2015.07.040.

64 T. Choudhury, S. O. Saied, J. L. Sullivan and A. M. Abbot, Reduction of oxides of iron, cobalt, titanium and niobium by low-energy ion bombardment, *J. Phys. D Appl. Phys.*, 1989, **22**, 1185–1195, DOI: 10.1088/0022-3727/22/8/026.

65 E. Arciga-Duran, Y. Meas, J. J. Perez-Bueno, J. C. Ballesteros and G. Trejo, Electrochemical synthesis of $Co_3O_4$-x films for their application as oxygen evolution reaction electrocatalysts: role of oxygen vacancies, *J. Electrochem. Soc.*, 2018, **165**, H3178–H3186, DOI: 10.1149/2.0261804jes.

66 J. G. Kim, D. L. Pugmire, D. Battaglia and M. A. Langell, Analysis of the $NiCo_2O_4$ spinel surface with Auger and X-ray photoelectron spectroscopy, *Appl. Surf. Sci.*, 2000, **165**, 70–84, DOI: 10.1016/S0169-4332(00)00378-0.

67 J. He, G. Tian, D. Liao, Z. Li, Y. Cui, F. Wei and C. Zhang, Mechanistic insights into methanol conversion and methanol-mediated tandem catalysis toward hydrocarbons, *J. Energy Chem.*, 2026, **112**, 778–803, DOI: 10.1016/j.jechem.2025.09.007.

68 Z. Wu, B. Yang, S. Miao, W. Liu, J. Xie, S. Lee, *et al.*, Lattice strained Ni-Co alloy as a high-performance catalyst for catalytic dry reforming of methane, *ACS Catal.*, 2019, **9**, 2693–2700, DOI: 10.1021/acscatal.8b02821.

69 L. Guo, W. Chen, C. Wang and B. Dong, Application of electrochemically assisted synthesis of MOFs-derived phosphides as catalyst for CH4-CO2 reforming, *Int. J. Electrochem. Sci.*, 2023, **18**(1), 26–32, DOI: 10.1016/j.ijoes.2023.01.005.

70 Y. Wang, Y. Liu, Z. Lin, H. Sun, Z. Cheng, K. Wang and D. Huang, Particle Dynamics and Wear Characteristics of Lining Layers in Curved Non-metallic Flexible Pipes for Deep-Sea Mining, *Pet. Sci.*, 2025, **23**, 447–463, DOI: 10.1016/j.petsci.2025.11.015.

71 X. Zhang, C. Yang, Y. Zhang, Y. Xu, S. Shang and Y. Yin, Ni-Co catalyst derived from layered double hydroxides for dry reforming of methane, *Int. J. Hydrogen Energy*, 2015, **40**, 16115–16126, DOI: 10.1016/j.ijhydene.2015.09.150.

72 T. Nejat, P. Jalalinezhad, F. Hormozi and Z. Bahrami, Hydrogen production from steam reforming of ethanol over Ni-Co bimetallic catalysts and MCM-41 as support, *J. Taiwan Inst. Chem. Eng.*, 2019, **97**, 216–226, DOI: 10.1016/j.jtice.2019.01.025.

73 Y. Wang, Y. Hu, K. Zhang, W. An, H. Zhou, Z. Lin and S. F. Estefen, The impact of filament winding configurations on the ultimate load-bearing capacity of non-metallic flexible pipes, *Ocean. Eng.*, 2025, **341**, 122516, DOI: 10.1016/j.oceaneng.2025.122516.

74 L. Li, D. H. Anjum, H. Zhu, Y. Saih, P. V. Laveille, L. D'Souza, *et al.*, Synergetic effects leading to coke-resistant NiCo bimetallic catalysts for dry reforming of methane, *ChemCatChem*, 2015, **7**, 427–433, DOI: 10.1002/cctc.201402921.

75 Y. Xu, S. Chen, L. Yao, W. Dai, J. Fang, C. Sun, W. Feng, J. Zou and X. Luo, Janus Mn single atoms for triggering efficient photothermal catalytic CO2 methanation through spin polarization effect, *Sci. Adv.*, 2026, **12**(1), eadz7504, DOI: 10.1126/sciadv.adz7504.

76 D. San-Jose-Alonso, J. Juan-Juan, M. J. Illan-Gomez and M. C. Roman-Martínez, Ni, Co and bimetallic NiCo catalysts for the dry reforming of methane, *Appl. Catal., A*, 2009, **371**, 54–59, DOI: 10.1016/j.apcata.2009.09.026.

77 L. Huang, X. Jiao, J. Lin, J. Hao, L. Tan, D. Zeng and F. Yan, EGDE-induced crosslinking of PEI@D500 adsorbents for direct air capture: Enhanced hydrothermal and oxidative stability, *Chem. Eng. J.*, 2026, **537**, 176243, DOI: 10.1016/j.cej.2026.176243.

78 J. Shen, A. A. C. Reule and N. Semagina, Ni/MgAl2O4 catalyst for low temperature oxidative dry methane reforming with CO2, *Int. J. Hydrogen Energy*, 2019, **44**, 4616–4629, DOI: 10.1016/j.ijhydene.2019.01.027.

79 X. Y. Quek, D. Liu, W. N. E. Cheo, H. Wang, Y. Chen and Y. Yang, Nickelgrafted TUD-1 mesoporous catalysts for carbon dioxide reforming of methane, *Appl. Catal., B*, 2010, **95**, 374–382, DOI: 10.1016/j.apcatb.2010.01.016.

80 G. Moradi, F. Khezeli and H. Hemmati, Syngas production with dry reforming of methane over Ni/ZSM-5 catalysts, *J. Nat. Gas Sci. Eng.*, 2016, **33**, 657–665, DOI: 10.1016/j.jngse.2016.06.004.

81 O. Omoregbe, H. T. Danh, C. Nguyen-Huy, H. D. Setiabudi, S. Z. Abidin, Q. D. Truong, *et al.*, Syngas production from methane dry reforming over Ni/SBA-15 catalyst: effect of operating parameters, *Int. J. Hydrogen Energy*, 2017, **42**, 11283–11294, DOI: 10.1016/j.ijhydene.2017.03.146.

82 K. V. Manukyan, A. Avetisyan, C. Shuck, S. Rouvimov and S. Kharatyan, Nickel oxide reduction by hydrogen: kinetics and structural transformations, *J. Phys. Chem. C*, 2015, **19**(28), 16131–16138, DOI: 10.1021/acs.jpcc.5b04313.

83 S. L. Kharatyan and H. A. Chatilyan, Kinetics and mechanism of nickel oxide reduction by methane, *J. Phys. Chem. C*, 2019, **123**(35), 21513–21521, DOI: 10.1021/acs.jpcc.9b04506.

84 J. Estephane, S. Aouad, S. Hany, B. El Khoury, C. Gennequin, H. El Zakhem, *et al.*, CO2reforming of methane overNi-Co/ZSM5 catalysts. Aging and carbon deposition study, *Int. J. Hydrogen Energy*, 2015, **40**, 9201–9208, DOI: 10.1016/j.ijhydene.2015.05.147.

85 Y. Fu, H. Yu, C. Jiang, T. Zhang, R. Zhan, X. Li, *et al.*, NiCo alloy nanoparticles decorated on N-doped carbon nanofibers as highly active and durable oxygen, *Electrocatalyst*, 2018, 1–10, DOI: 10.1002/adfm.201705094.1705094.

86 J. L. Pinilla, S. de Llobet, R. Moliner and I. Suelves, Ni-Co bimetallic catalysts for the simultaneous production of carbon nanofibres and syngas through biogas decomposition, *Appl. Catal., B*, 2017, **200**, 255–264, DOI: 10.1016/j.apcatb.2016.07.015.

87 J. Xu, W. Zhou, Z. Li, J. Wang and J. Ma, Biogas reforming for hydrogen production over a Ni-Co bimetallic catalyst: effect of operating conditions, *Int. J. Hydrogen Energy*, 2010, **35**, 13013–13020, DOI: 10.1016/j.ijhydene.2010.04.075.

88 X. Chen, S. Cai, E. Yu, J. Li, J. Chen and H. Jia, Photothermocatalytic performance of $ACo_2O_4$ type spinel with light-enhanced mobilizable active oxygen species for toluene oxidation, *Appl. Surf. Sci.*, 2019, **484**, 479–488, DOI: 10.1016/j.apsusc.2019.04.093.

89 M. Nemeth, Z. Schay, D. Sranko, J. Karolyi, G. Safran, I. Sajo, *et al.*, Impregnated $Ni/ZrO_2$ and Pt/ZrO2 catalysts in dry reforming of methane: activity tests in excess methane and mechanistic studies with labeled $13CO_2$, *Appl. Catal., A*, 2015, **504**, 608–620, DOI: 10.1016/j.apcata.2015.04.006.

90 Å. Björkman, Thermische Klärschlammbehandlung, *Schweiz. Z. Hydrol.*, 1969, **31**, 632–645, DOI: 10.1007/BF02543692.